General Disclaimer

One or more of the Following Statements may affect this Document

- This document has been reproduced from the best copy furnished by the organizational source. It is being released in the interest of making available as much information as possible.

- This document may contain data, which exceeds the sheet parameters. It was furnished in this condition by the organizational source and is the best copy available.

- This document may contain tone-on-tone or color graphs, charts and/or pictures, which have been reproduced in black and white.

- This document is paginated as submitted by the original source.

- Portions of this document are not fully legible due to the historical nature of some of the material. However, it is the best reproduction available from the original submission.

DRA

KWLCX

SPECTRAL EMISSIVITY OF METALS AFTER DAMAGE BY PARTICLE IMPACT

FINAL REPORT

Prepared by

Tibor S. Laszlo
Richard E. Gannon

RESEARCH AND ADVANCED DEVELOPMENT DIVISION
AVCO CORPORATION
Wilmington, Massachusetts

Technical Report
RAD-TR-63-39
Contract NAS 8-1642

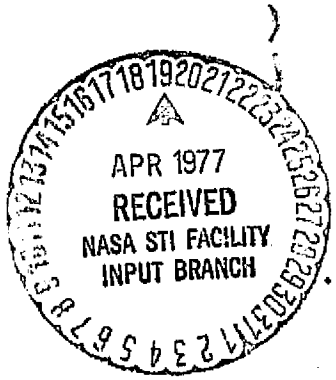

5 September 1963

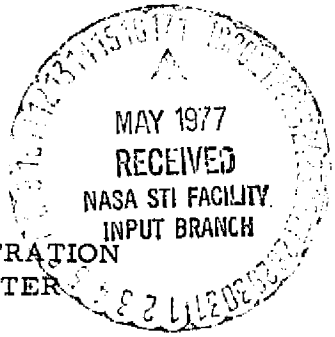

Prepared for

NATIONAL AERONAUTICS AND SPACE ADMINISTRATION
GEORGE C. MARSHALL SPACE FLIGHT CENTER
Huntsville, Alabama

NASA-

This document consists of 70 pages,
100 copies, Series A

SPECTRAL EMISSIVITY OF METALS AFTER DAMAGE BY PARTICLE IMPACT

FINAL REPORT

Prepared by

Tibor S. Laszlo
Richard E. Gannon

RESEARCH AND ADVANCED DEVELOPMENT DIVISION
AVCO CORPORATION
Wilmington, Massachusetts

Technical Report
RAD-TR-63-39

Contract NAS 8-1642

5 September 1963

Prepared for

NATIONAL AERONAUTICS AND SPACE ADMINISTRATION
GEORGE C. MARSHALL SPACE FLIGHT CENTER
Huntsville, Alabama

ABSTRACT

The reflectance, R, solar absorptance, α, thermal emittance, ϵ, and the α/ϵ ratio were determined for several metals before and after bombardment by high velocity microprojectiles. Observed decreases of 1 to 26 percent in the reflectance of various metals were apparently dependent on the amount of surface area damaged as well as on the velocity of the impinging projectiles. The thermal emittance was observed to increase more than the solar absorptance, which resulted in a net decrease in the α/ϵ ratio in all metals investigated except stainless steel 304. In the case of stainless steel 304, α and ϵ were observed to increase equally, resulting in an α/ϵ ratio apparently insensitive to microprojectile bombardment. Recommendations for the continuation of these investigations are outlined.

CONTENTS

I. Introduction 1

A. Theoretical Background 1
B. Experimental Methods 4

II. Results and Analysis 25

III. Conclusions and Recommendations 67

A. Conclusions 67
B. Recommendations 67

IV. References 69

ILLUSTRATIONS

Figure	1	Penetration versus Velocity for Metal-to-Metal Impacts with Associated Shapes	5
	2	Zircaloy Particles Used to Simulate Micrometeorites	6
	3	Microparticle Sabot	7
	4	Schematic of Microparticle Range	7
	5	Schematic of High-Velocity Microparticle Accelerator	8
	6	Tungsten Projectiles	9
	7	Strip Film for Calculation of Projectile Velocities	11
	8	Impacted Gold Specimen	12
	9	Photomicrograph of Cross Section of Impacted Gold Specimen	13
	10	Modified Optical System	15
	11	Hohlraum and Transfer Optics	16
	12	Magnitude of Errors	17
	13	Apparatus for Measuring α/ϵ	18
	14	Correlation Between Incident Flux and External Thermopile Output	23
	15	Distribution of Crater Diameters in Impacted Aluminum (Shot 53) -- Reflectance Specimen, 5000 ft/sec (1500 m/sec) Projectiles	27
	16	Distribution of Crater Diameters in Impacted Gold (Shot 67) -- Reflectance Specimen, 5000 ft/sec (1500 m/sec) Projectiles	28
	17	Distribution of Crater Diameters in Impacted Stainless Steel, Type 304 (Shot 46) -- Reflectance Specimen, 5000 ft/sec (1500 m/sec) Projectiles	29

ILLUSTRATIONS (Cont'd)

Figure 18 Distribution of Crater Diameters in Impacted Chromium Plate (Shot 54) -- Reflectance Specimen, 5000 ft/sec (1500 m/sec) Projectiles 30

19 Distribution of Crater Diameters in Impacted Stainless Steel, Type 316 (Shot 47) -- Reflectance Specimen, 5000 ft/sec (1500 m/sec) Projectiles..... 31

20 Distribution of Crater Diameters in Impacted Silver (Shot 68) -- Reflectance Specimen, 5000 ft/sec (1500 m/sec) Projectiles 32

21 Distribution of Crater Diameters in Impacted Tungsten (Shots 65 and 66) -- Reflectance Specimen, 5000 ft/sec (1500 m/sec) Projectiles 33

22 Distribution of Crater Sizes in Impacted Aluminum -- Reflectance Specimen, 20,000 ft/sec (7000 m/sec) Projectiles 34

23 Distribution of Crater Sizes in Impacted Aluminum -- a/ϵ Specimen, 20,000 ft/sec (7000 m/sec) Projectiles 35

24 Distribution of Crater Sizes in Impacted Gold -- Reflectance Specimen, 17,000 ft/sec (5200 m/sec) Projectiles..... 36

25 Distribution of Crater Sizes in Impacted Gold -- a/ϵ Specimen, 20,000 ft/sec (7000 m/sec) Projectiles 37

26 Distribution of Crater Sizes in Impacted Stainless Steel, Type 304 -- Reflectance Specimen, 20,000 ft/sec (7000 m/sec) Projectiles 38

27 Distribution of Crater Sizes in Impacted Stainless Steel, Type 304 -- a/ϵ Specimen, 20,000 ft/sec (7000 m/sec) Projectiles..... 39

28 Distribution of Crater Sizes in Impacted Platinum -- Reflectance Specimen, 20,000 ft/sec (7000 m/sec) Projectiles 40

ILLUSTRATIONS (Cont'd)

Figure 29 Distribution of Crater Sizes in Impacted Platinum -- α/ϵ Specimen 20,000 ft/sec (7000 m/sec) Projectiles 41

30 Distribution of Crater Sizes in Impacted Chromium-Plated Copper -- Reflectance Specimen, 20,000 ft/sec (7000 m/sec) Projectiles 42

31 Distribution of Crater Sizes in Impacted Chromium-Plated Copper -- α/ϵ Specimen, 20,000 ft/sec (7000 m/sec) Projectiles 43

32 Composite Photograph of Aluminum Specimens Damaged by High and Low Velocity Projectiles; A--5000 ft/sec (1500 m/sec), B--20,000 ft/sec (7000 m/sec)..... 44

33 Composite Photograph of Gold Specimens Damaged by High and Low Velocity Projectiles; A--5000 ft/sec (1500 m/sec), B--20,000 ft/sec (7000 m/sec)..... 45

34 Composite Photograph of Stainless Steel 304 Specimens Damaged by High and Low Velocity Projectiles; A--5000 ft/sec (1500 m/sec), B--20,000 ft/sec (7000 m/sec)..... 46

35 Composite Photograph of Chromium-Plated Copper Specimens Damaged by High and Low Velocity Projectiles; A--5000 ft/sec (1500 m/sec), B--20,000 ft/sec (7000 m/sec)..... 47

36 Spectral Reflectance of Aluminum 51

37 Spectral Reflectance of Gold 52

38 Spectral Reflectance of Stainless Steel, Type 304..... 53

39 Spectral Reflectance of Platinum 54

40 Spectral Reflectance of Chromium-Plated Copper 55

41 Spectral Reflectance of Silver..... 56

42 Spectral Reflectance of Tungsten 57

ILLUSTRATIONS (Concl'd)

Figure 43 Spectral Reflectance of Stainless Steel, Type 316..... 58

44 α/ϵ of Aluminum 59

45 α/ϵ of Gold 60

46 α/ϵ of Stainless Steel, Type 304..... 61

47 α/ϵ of Platinum 62

48 α/ϵ of Chromium-Plated Copper 63

TABLES

Table I Description of Damage to Specimens 26

II Reflectance Before and After Impact by 5000 ft/sec (1500 m/sec) Zircaloy Particles 49

III Reflectance Before and After Impact by 20,000 ft/sec (7000 m/sec) Zircaloy Particles 50

IV Effect of Micrometeorite Impacts on Optical Properties 65

V Comparison of Orders of Optical and Surface Changes 66

I. INTRODUCTION

The radiation parameters of the vehicle skin greatly affect the energy passage to and from space vehicles. These parameters, in turn, vary with the physical conditions of the surface. A most important factor in altering the quality of the original surface is micrometeorite impact. It is necessary, therefore, to determine such effects by simulating the micrometeorite impact in the laboratory and to measure the consequent change in radiation parameters.

Recognizing this need, the George C. Marshall Space Flight Center, NASA, awarded contract NAS 8-1642 to Avco RAD on 5 June 1961 for the Investigation of Spectral Emissivity of Metals after Damage by Particle Impact. This contract called for the measurement of the spectral emissivity of selected metals and for the determination of the effect of simulated micrometeorite impact on the emissivity of metal surfaces. The contract, originally written for 1 year, has been extended through 5 September 1963. Added to the original program was the determination of the ratio of solar absorptance to thermal emittance, for the selected metals in the temperature range -65 to 140 °C, and the measurement of the change of this ratio after microparticle impact.

For administrative reasons, a "final" report on this work was issued on 13 August 1962. The present report includes that material of the previous report which proved to be pertinent to the final results and to the evaluation of the problem.

The work on this contract was initiated by Charles H. Leigh as principal investigator assisted by Stanely Wolnik. In December 1962, the responsibility for the work was transferred to Tibor S. Laszlo (principal investigator), Richard E. Gannon, and Albert Bothe. The impacting facility was developed by J. Eckerman and W. McKay.

A. THEORETICAL BACKGROUND

Several authors[1, 2, 3] have demonstrated the effect of optical properties of a satellite on its equilibrium temperature.

The following expression, derived by Hass, Drummeter, and Schach[1] illustrates the importance of optical properties in the calculation of the equilibrium temperature of an orbiting satellite.

$$(P_s + P_a)\, a/\epsilon + P_\epsilon = A\sigma T_m^4 \qquad (1)$$

where

P_s = direct solar radiation incident on the satellite

P_a = earth-reflected solar radiation incident on the satellite

P_ℓ = earth-emitted radiation incident on the satellite

α = solar absorptance of the shell

ϵ = thermal emittance of the shell

A = surface area of the shell

σ = Stefan-Boltzmann constant

T_m = mean orbital shell temperature.

Other authors[4, 5, 6] have recognized, at least qualitatively, the effect of surface roughness on the optical properties of materials. From these studies, it follows that a process, such as micrometeorite bombardment, that would alter the original surface of a satellite, would also alter its equilibrium temperature. Since there is no presently available information on the effect of micrometeorite bombardment on the surface finish of a satellite, or any quantitative correlation between changes in surface roughness and changes in optical properties, it became important to simulate the effect of micrometeorite impacts on candidate skin materials and to determine the resulting change in optical properties.

To further illustrate that changes in surface roughness would effectively alter the optical properties of a satellite and consequently its thermal equilibrium, the following considerations are presented.

The total amount of solar radiation intercepted by a specimen depends on its surface area projection on a plane perpendicular to the axis of solar radiation (the so-called shadow area). The total amount of emitted radiation, in contrast, depends on the effective radiating area, and on its shape, since radiation is emitted in all directions of space (2π). It can be seen that pits or cavities in the surface would affect the fraction of solar radiation absorbed by creating radiation "traps," and that they would affect the thermal emittance by effectively enlarging the emitting surface area.

A square specimen 1 cm on a side, for which the apparent macroscopic surface area is $A = 1\ cm^2$, might have a true (microscopic) surface area S equal to 5 or 10 times A, because of the effect of surface roughness. If it is assumed that each small element of the surface radiates like an ideal specimen of the material, then the total radiation emitted from the surface would be

$$\epsilon_o \sigma T^4 S = \frac{S}{A} \epsilon_o \sigma T^4 A \qquad (2)$$

where ϵ_o is the emittance of the undamaged surface.

Because of surface roughness, much of this emitted radiation would be reflected from the surface several times before it could escape. At each reflection, part of the radiation would be reabsorbed. For a surface having an area ratio $\frac{S}{A}$, the average number of times the radiation would be reflected from the surface before finally escaping would be approximately $\frac{S}{A} - 1$. Accordingly, the apparent emittance of this surface would be

$$\epsilon = \epsilon_o \frac{S}{A} T_o^{\left(\frac{S}{A} - 1\right)} = \epsilon_o \frac{S}{A} (1 - \epsilon_o)^{\left(\frac{S}{A} - 1\right)} \quad . \tag{3}$$

A better approximation for the effective emittance would take account of the fact that all the radiation emitted from a real surface is not reflected the same number of times; part of it escapes immediately without any reflection, part of it is reflected once, part of it twice, etc. Thus, if $f(n)$ represents the fraction of radiation reflected n times, then the effective emittance of the surface is given by

$$\epsilon = \epsilon_o \frac{S}{A} \sum_{n=0}^{\infty} f(n) (1 - \epsilon_o)^n \tag{4}$$

where ϵ_o is the emittance of the ideally smooth surface.

In accordance with Kirchoff's Law, the absorptivity is equal to the emittance for opaque materials, provided all energy traffic takes place by radiation. This correlation, however, applies only for cases when the absorbed and emitted radiation have identical spectral distribution. In the case under consideration, this is not so. The solar radiation impinging on the skin of a space vehicle has the spectral distribution approximating that of a blackbody at 6000°K with the peak at 0.48 μ. The emitted radiation, in turn, because of the necessarily much lower temperature of the vehicle (300 to 600°K) is mainly in the infrared with the peak above 4.5 μ. Since the skin material neither absorbs nor emits as a blackbody, the change in surface structure will affect first the fraction of solar radiation absorbed, then the temperature reached by the metal due to the absorbed energy. As the temperature increases, both the intensity and the spectral distribution of the emitted energy change. The intensity is further affected by the surface structure, as discussed above, and the spectral distribution is altered randomly because the surface is not a blackbody emitter.

Accordingly, for the evaluation of the changes in radiative characteristics of a material in space, the a/ϵ value has to be determined on a "new" (usually polished) surface, as well as on a surface bearing the simulated effects of all agents acting on it in space. In the present work, the effect of micrometeorite impact on selected metals was considered.

B. EXPERIMENTAL METHODS

1. Micrometeorite Simulation

Damage caused by micrometeorite impingement was simulated by exposing specimens to high velocity microparticles. In the initial phase of the program, the microparticles were accelerated to velocities of 5000 ft/sec (1500 m/sec) by means of a powder charge and ballistic launch tube assembly. Later, they were accelerated to 23,000 ft/sec (7800 m/sec) through the use of a light gas gun. Although this velocity is less than 25 percent of the estimated velocity of the slowest micrometeorites, the individual craters caused by their impacts are generally similar to craters caused by impacts of much higher velocity particles. This assumption is based on findings reported at the Fourth Symposium on Hypervelocity Impacts,[7] which showed that the general shape of craters caused by particle impacts is dependent upon the velocity of the impinging particle. Such craters can be divided into three categories corresponding to three projectile velocity regions (figure 1). Since the velocity of the microparticles used in the later phases of the program were well within the hypervelocity region, which presumably includes the velocities of micrometeorites, it was concluded that the general shape of the craters formed by the impacts of particles traveling at 20,000 ft/sec (6800 m/sec) would be similar to those caused by micrometeorites traveling at 100,000 ft/sec (34,000 m/sec) or more.

A 0.220 caliber powder gun was used to achieve velocities of approximately 5000 ft/sec (1500 m/sec) for the impinging particles in the initial state of the program. Zircoloy microspheres, 85 to 100μ in diameter (figure 2), were encapsulated in a plastic holder or "sabot" (figure 3). The sabot was positioned at the end of a 2-inch long launch tube and accelerated by a powder charge exploded in the compression chamber. The sabot was removed by a specially designed stripper at the entrance to the vacuum chamber releasing the encapsulated particles at a uniform initial velocity. The specimen was mounted at the opposite end of the vacuum chamber, facing the launch tube orifice. The velocity of the particles, just prior to impact, was measured with a speed graphic and a rotating drum camera. A schematic of the powder gun and accompanying equipment is shown in figure 4.

In the second stage of the program, a 0.220 caliber light gas gun was modified to accelerate particles to velocities as high as 23,000 ft/sec (7800 m/sec). The gun (figure 5) was loaded with a charge of 80 to 100μ diameter tungsten microparticles (figure 6) contained in a thin plastic envelope. The driver gas was compressed to high pressures and temperature first mechanically, and then by the detonation of a powder charge. At a predetermined pressure, a valve directly behind the powder charge was activated, exposing the charge to the high-pressure high-temperature gas. The plastic envelope was vaporized immediately and the tungsten particles were accelerated through an evacuated chamber toward the target. The

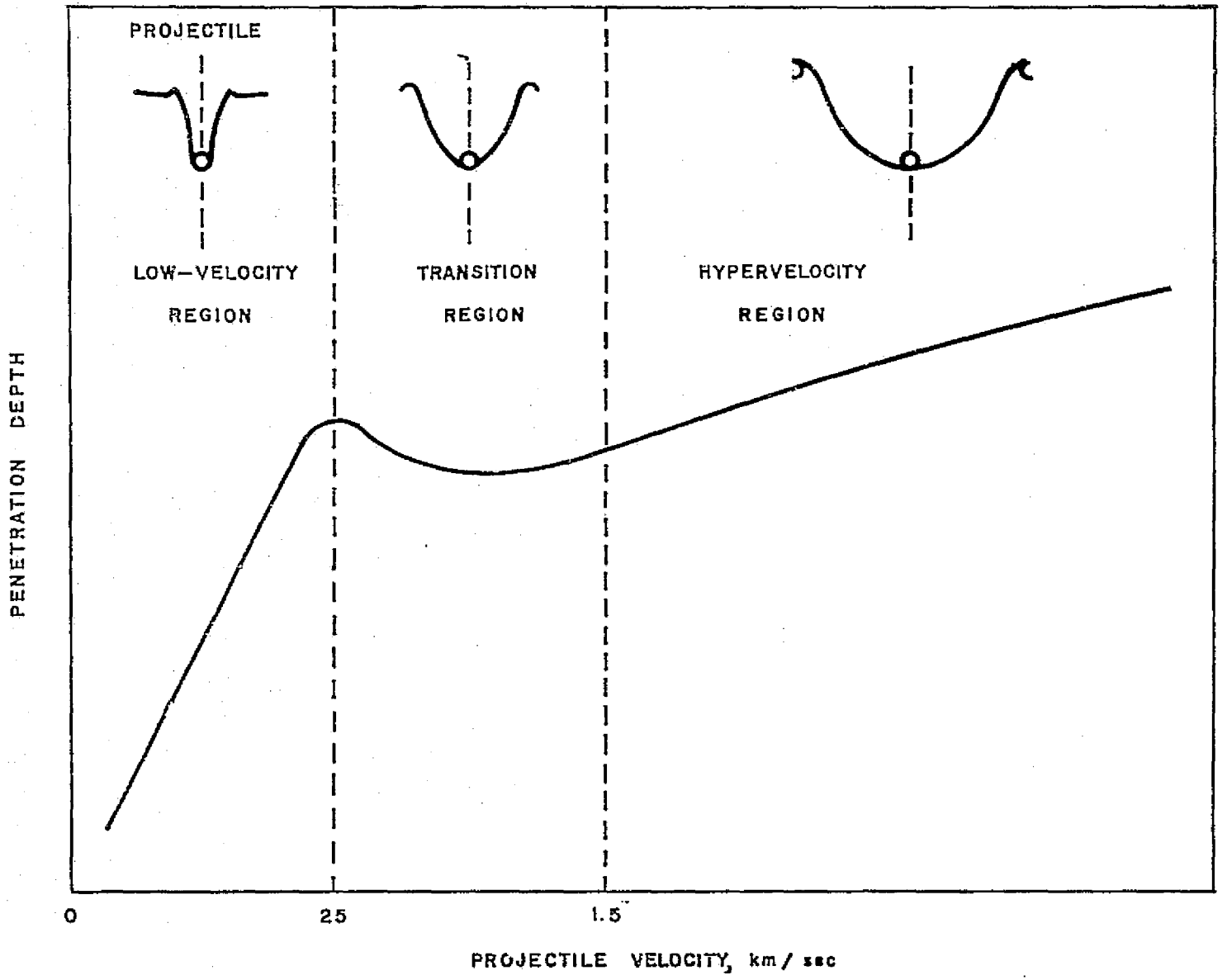

Figure 1 PENETRATION VERSUS VELOCITY FOR METAL-TO-METAL IMPACTS WITH ASSOCIATED SHAPES
62-6167

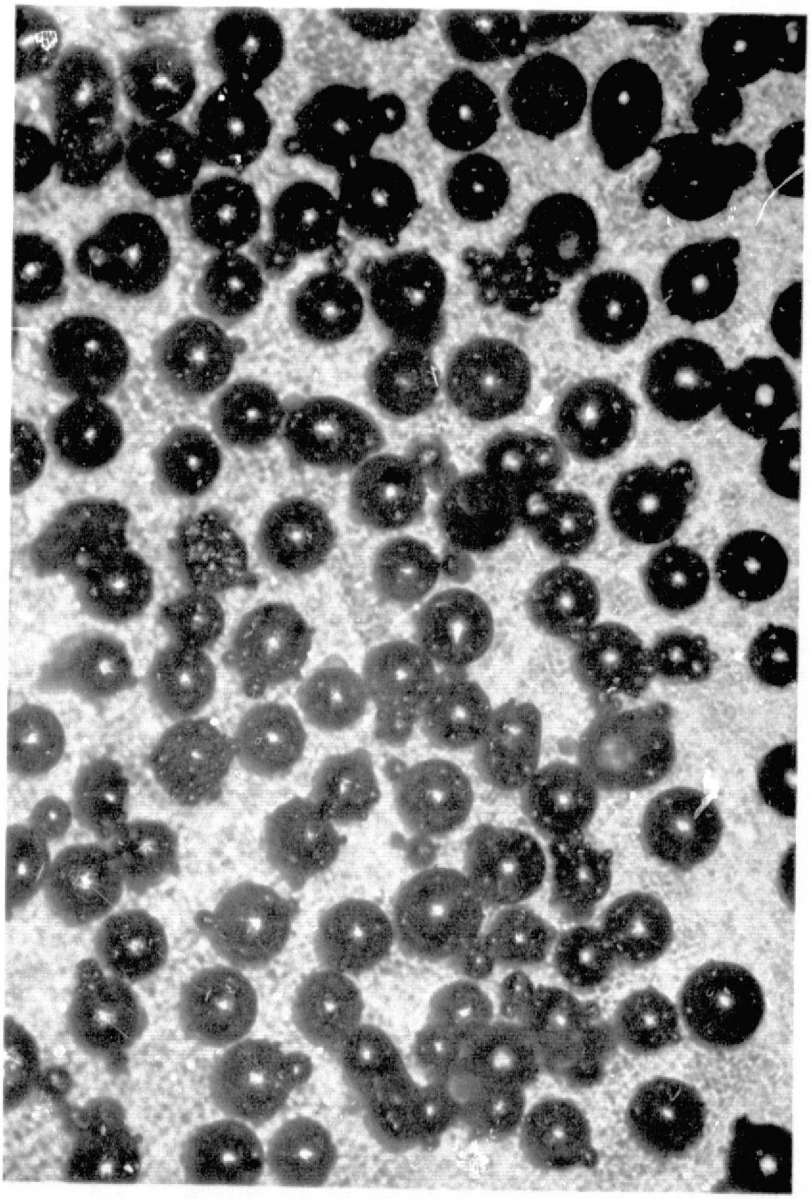

PLATE 3337 100X

63-10791

Figure 2 ZIRCALOY PARTICLES USED TO SIMULATE MICROMETEORITES

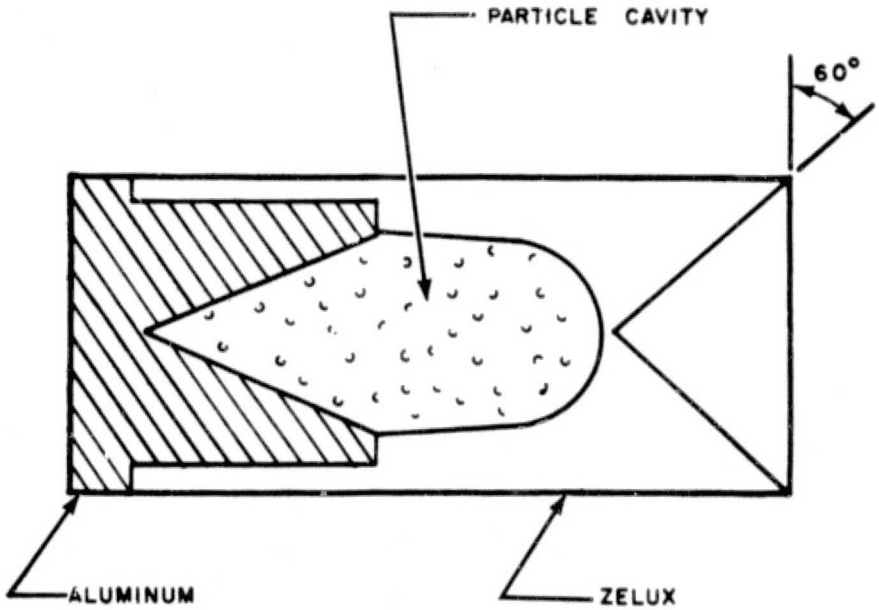

Figure 3 MICROPARTICLE SABOT
62-6191

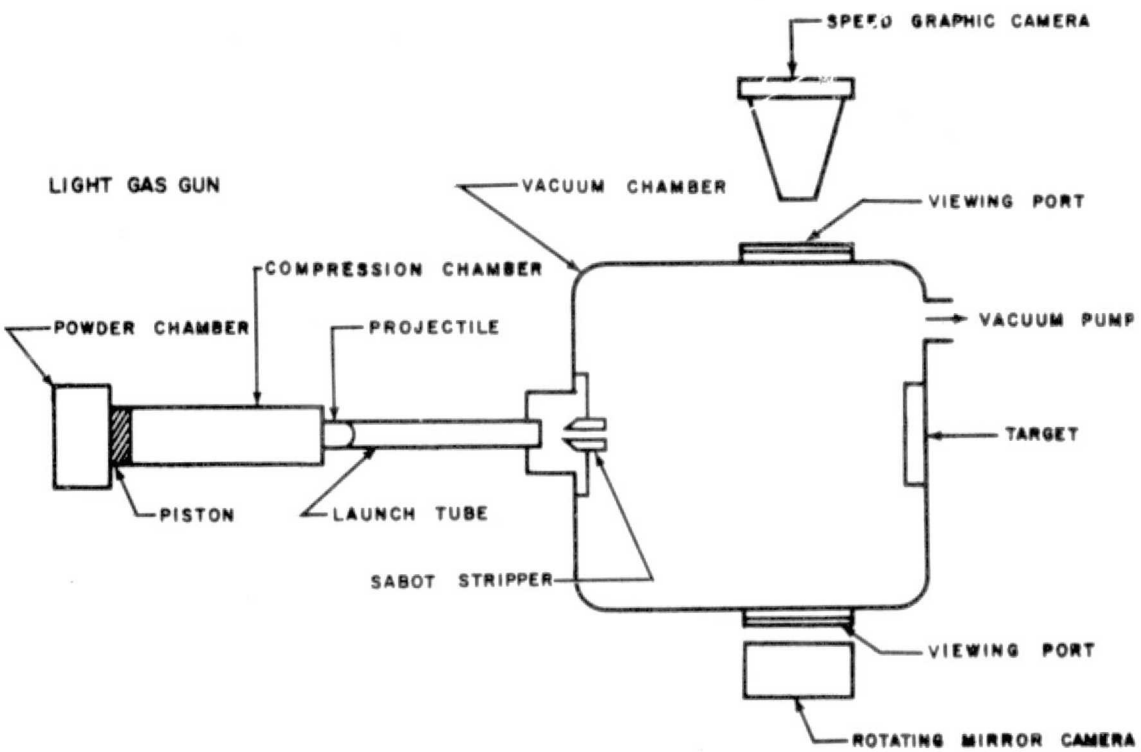

Figure 4 SCHEMATIC OF MICROPARTICLE RANGE
62-6190

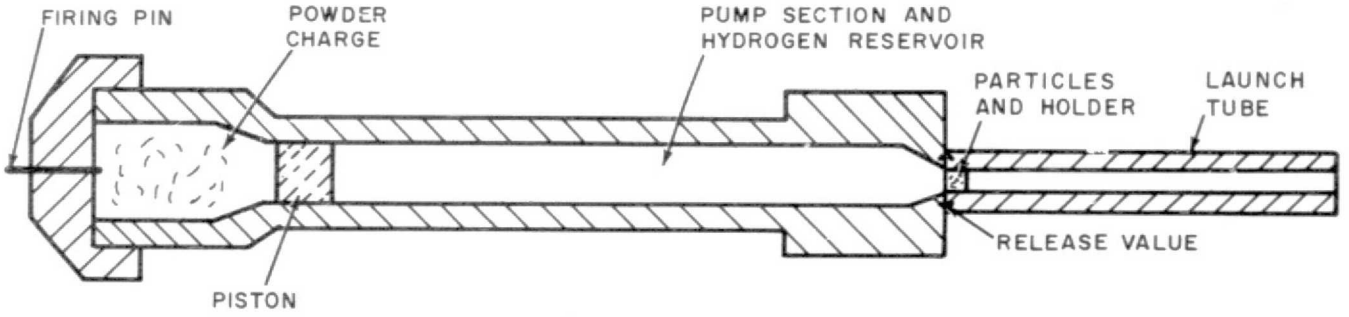

Figure 5 SCHEMATIC OF HIGH-VELOCITY MICROPARTICLE ACCELERATOR
63-8006

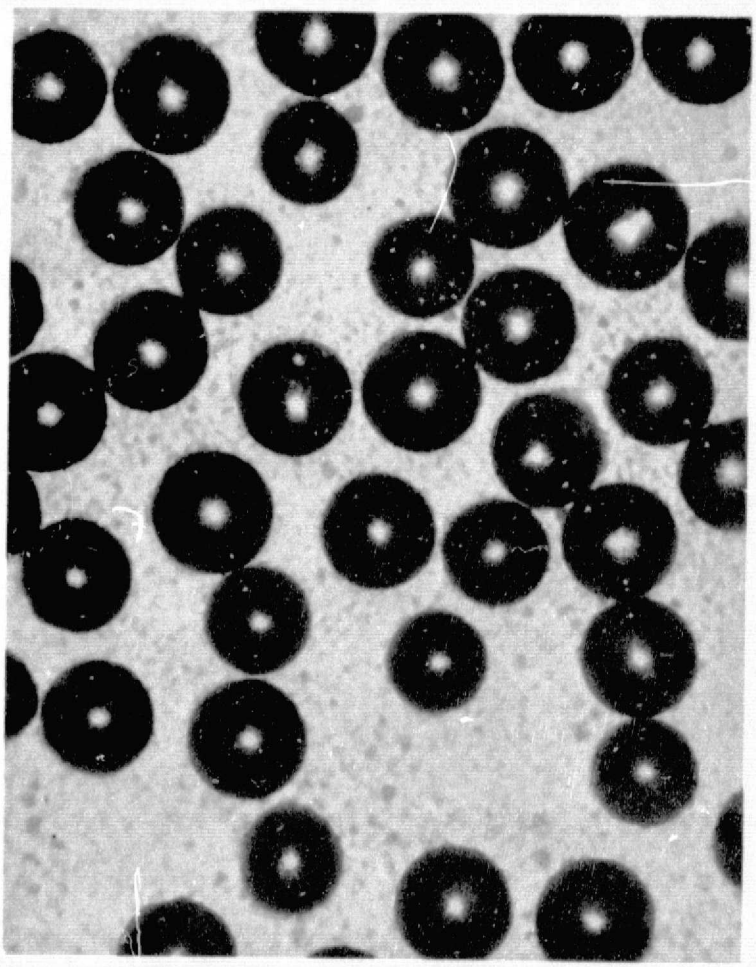

PLATE 3188A 150X

63-10766

Figure 6 TUNGSTEN PROJECTILES

velocity of the particles, just prior to impact, was measured by photographing the luminous streaks of individual particles with a rotating drum camera. A strip film from the rotating drum camera showing the luminous streaks is shown in figure 7. The velocity of the individual particles can be calculated from the knowledge of the diameter and speed of the camera, and a measurement of the angle of inclination of the streak on the film. Analysis of the films indicates an average velocity of 19 500 ± 1, 500 ft/sec (5900 ± 500 m/sec) (17, 000 ± 1, 500 ft/sec (5200 ± 500 m/sec) in the case of gold).

Figure 8 is a photomicrograph of a gold specimen after bombardment by the high velocity (~ 17, 000 ft/sec (5200 m/sec)) tungsten microparticles. The α/ϵ specimens were first bombarded on one side, turned over, and bombarded on the other side. Figure 9 is a photomicrograph of a cross sectional area of the impacted gold specimen showing a profile of two of the craters.

2. Surface Characterization

There are no acceptable standard procedures for the characterization and unequivocal definition of solid surfaces. (In addition, the lack of uniformity of the impacted surfaces only served to complicate the problem.) Both interference microscopy and profilometry were tried and found to be inadequate due to the difficulty in adapting them to the measurement of relatively large surfaces and to craters larger than 100 μ. Consequently, a technique of measuring the diameters and depths of a representative number of individual craters by means of a microscope was adopted. The distribution of crater sizes thus obtained was assumed to be representative of all the craters in a given material.

In the initial phase of the program, during impacting with 5000 ft/sec (1500 m/sec) particles, it was thought necessary to randomly select a representative number of craters for measurement. In the case of the specimens impacted in the light gas gun, however, the large number of craters and wide distribution of sizes made the adoption of a statistical sampling technique necessary. Accordingly, greatly enlarged photographs (20X) of the impacted disks were divided into nine 40-degree segments. Three segments were randomly selected for precise measurements of the number and diameter of all the craters observed. The results were then extrapolated to include the entire surface.

To test the validity of the sampling technique, the craters in three 40-degree segments of a specimen were counted. The results showed counts of 255, 253, and 285 craters for an average of 264 craters per segment, indicating a total 2376 craters for the entire surface. The craters in all the segments were then counted and found to total 2436. The difference of 60 in about 2400 is well within the bounds of the expected error in counting numbers of this magnitude.

FOREIGN PARTICLES TUNGSTEN PROJECTILES

P9954

Figure 7 STRIP FILM FOR CALCULATION OF PROJECTILE VELOCITIES

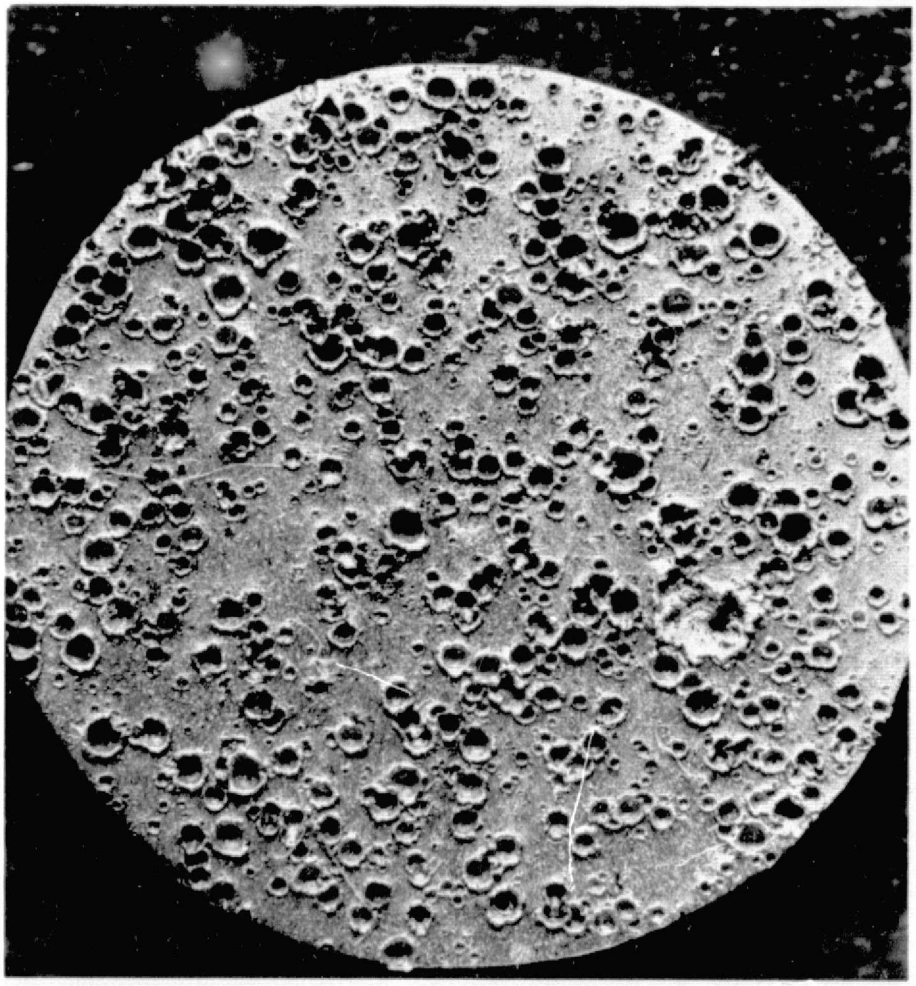

PL-3177-F 9X

Figure 8 IMPACTED GOLD SPECIMEN

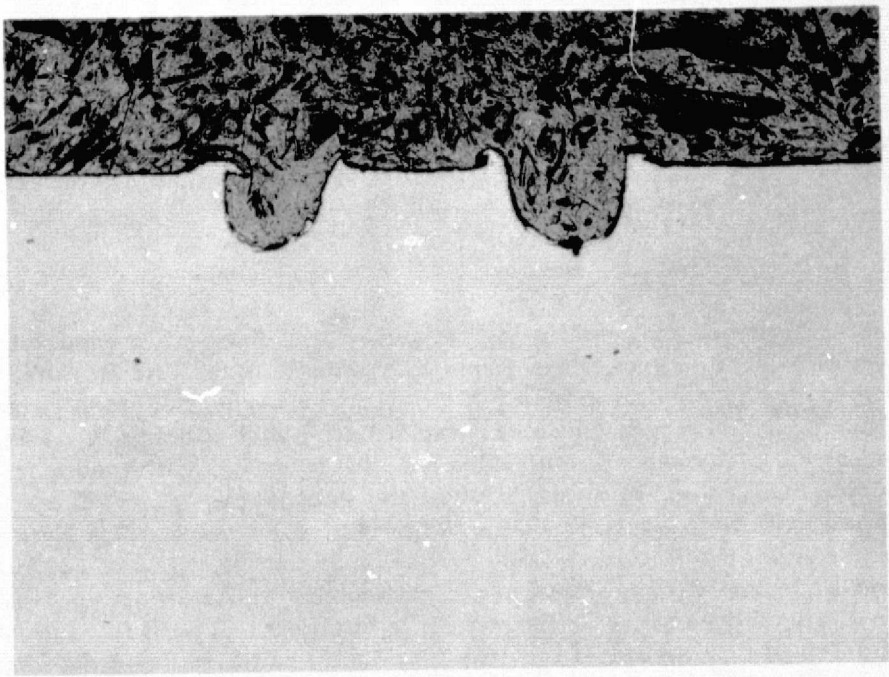

PLATE 3212C 100X

63-10767

Figure 9 PHOTOMICROGRAPH OF CROSS SECTION OF IMPACTED GOLD SPECIMEN

The diameter of each crater in the selected segments was measured on the enlarged photograph with a micrometer eyepiece. The average diameter of the craters was calculated from this tabulation. The depths of the craters were measured with an Ultraphot microscope. The microscope was first focused on the upper edge of the crater and then again on the bottom. The distance between the two foci as indicated on a micrometer scale was taken as the crater depth. The determination of the average depth of the craters by the sampling technique employed in determining the average diameter was rejected because of the time required for each depth measurement. Instead, the depth-to-diameter ratio of the craters in each material was established by a limited number of accurate depth and diameter measurements. Since, theoretically,[7] this ratio is constant for a given material impacted by particles of a uniform velocity, the distribution of depths was calculated from this ratio and the previously determined diameter distribution.

3. Reflectance Measurements

The reflectivity of the specimens between 2 and 25μ was measured by a method similar to the one described by Gier, Dunkle, and Bevans.[8] In this method, the specimen was placed within a blackbody enclosure, or Hohlraum, so that it was uniformly irradiated with blackbody radiation from a solid angle of 2π steradians. The blackbody was maintained at a constant temperature between 1100 and 1300°C for each series of readings and the specimen was maintained at room temperature by means of a water-cooled specimen holder. The blackbody radiation from the walls of the Hohlraum was reflected by the specimen and directed through a small aperture into an infrared spectrophotometer for spectral analysis. The Hohlraum was then rotated 180 degrees so that now the blackbody radiation was directed into the spectrophotometer for direct comparison of the radiation incident at, and reflected by, the sample. Measurements of both the incident and reflected radiation were made at 1μ intervals from 2 to 25μ. A diagram of the experimental setup is presented in figure 10 and a photograph of the Hohlraum, the transfer optics, and the spectrophotometer is shown in figure 11.

The errors inherent in this method of measuring infrared reflectance are discussed by Dunkle, Ehrenburg, and Gier.[9] An error may be caused by specimen emission if it is heated above room temperature. This error will be small for the highly polished metals but could be appreciable for the impacted specimens. Efficient water cooling of the specimen and instantaneous radiation measurements must, therefore, be relied on to minimize the self-emission error. Figure 12 shows the ratio of the error to the spectral emittance as a function of wavelength for a 27.8°K rise in specimen temperature at a Hohlraum temperature of 1400°F. It can be seen that this value is negligible at wavelength less than 10μ but that it increases to about 0.035 at 25μ.

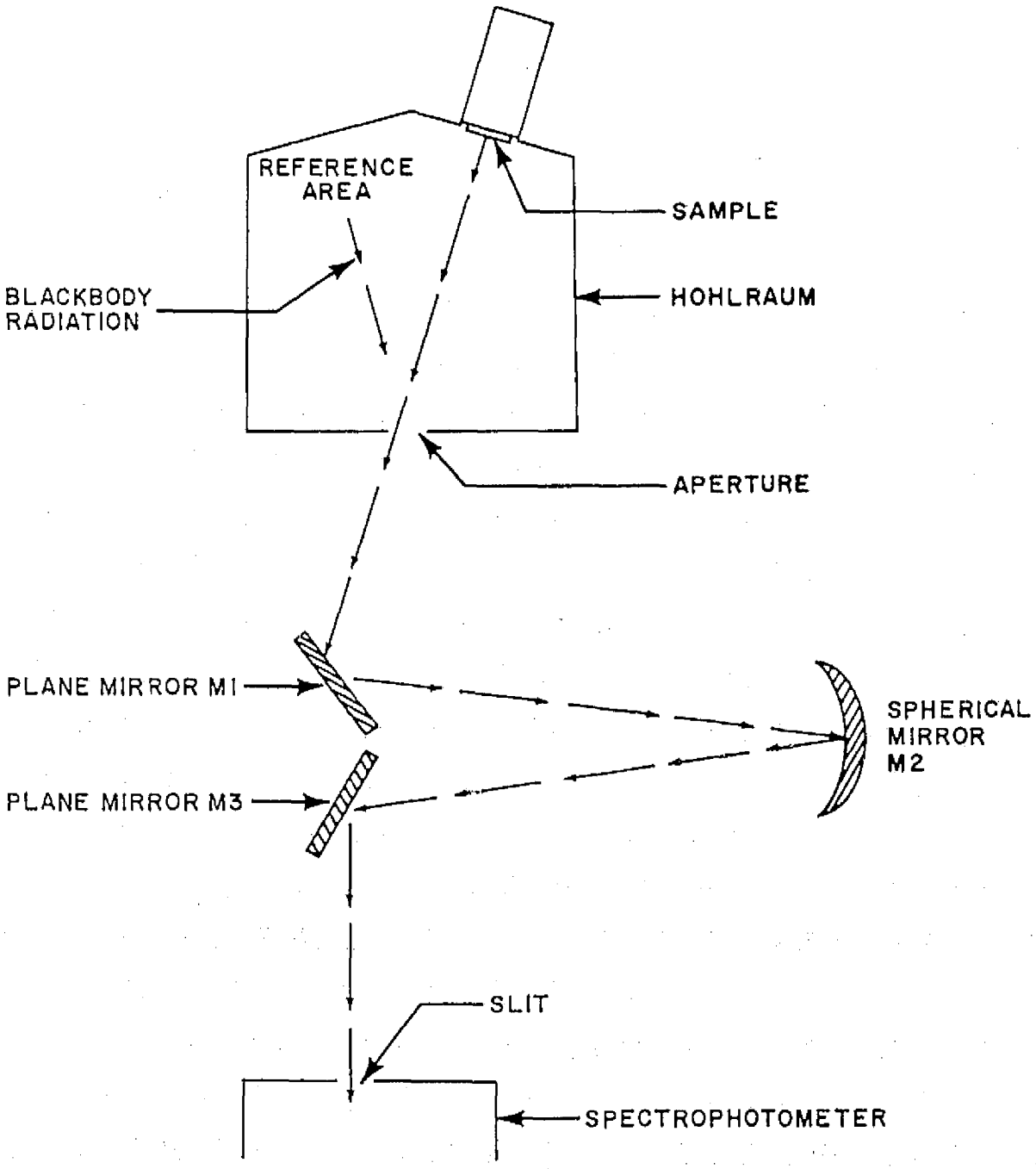

Figure 10 MODIFIED OPTICAL SYSTEM
61-2370

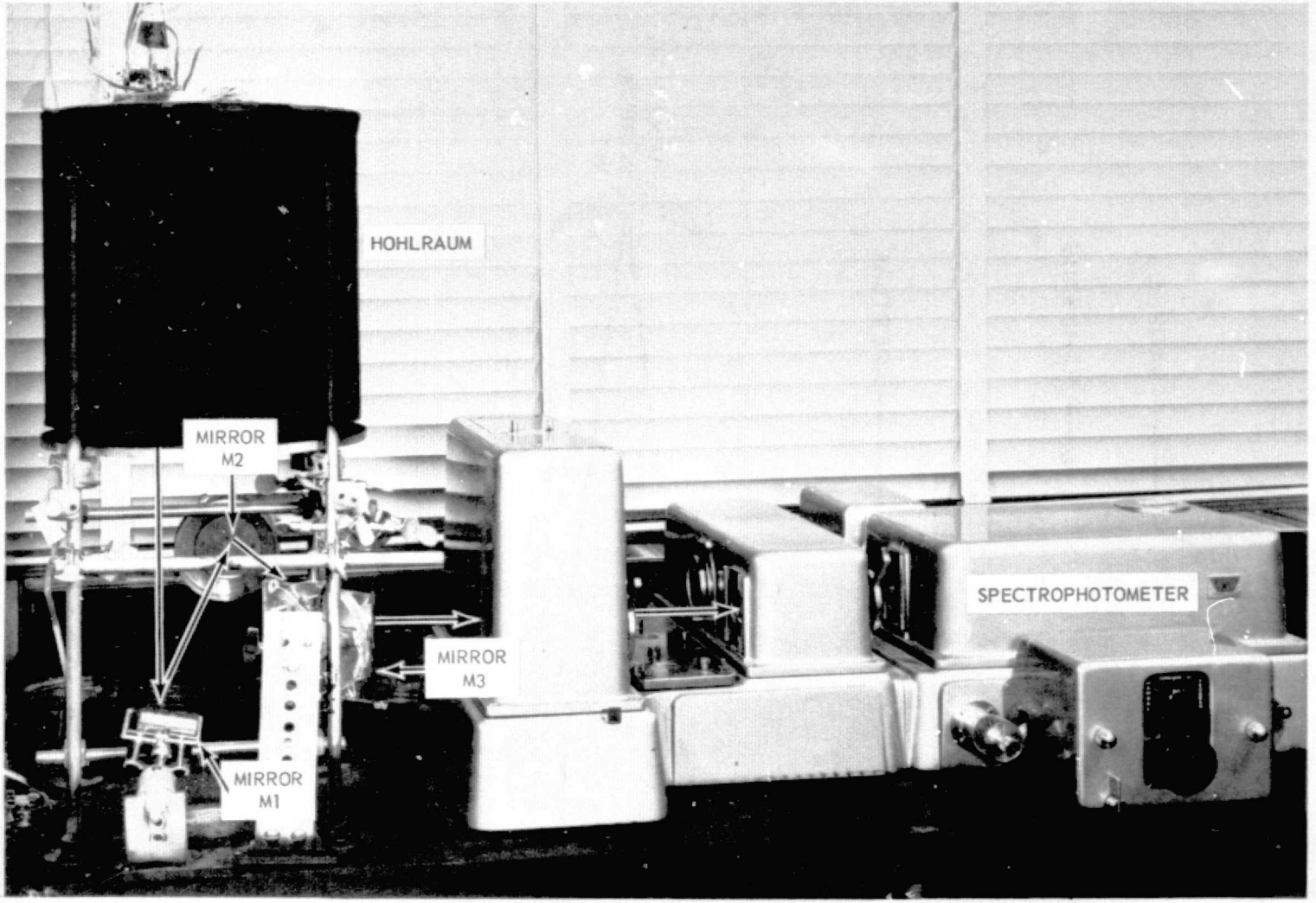

Figure 11 HOHLRAUM AND TRANSFER OPTICS
P6432B

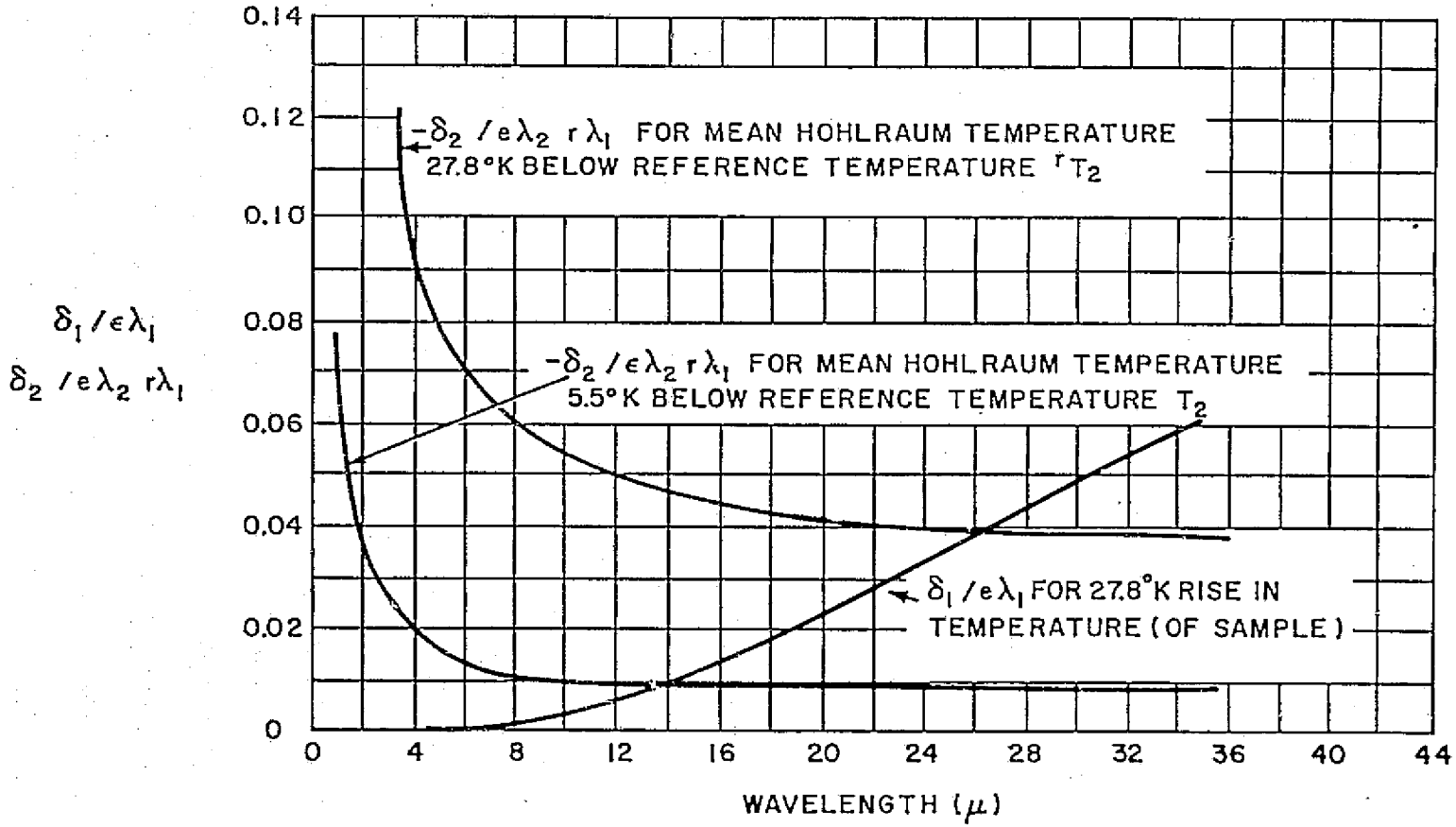

Figure 12 MAGNITUDE OF ERRORS
61-2371

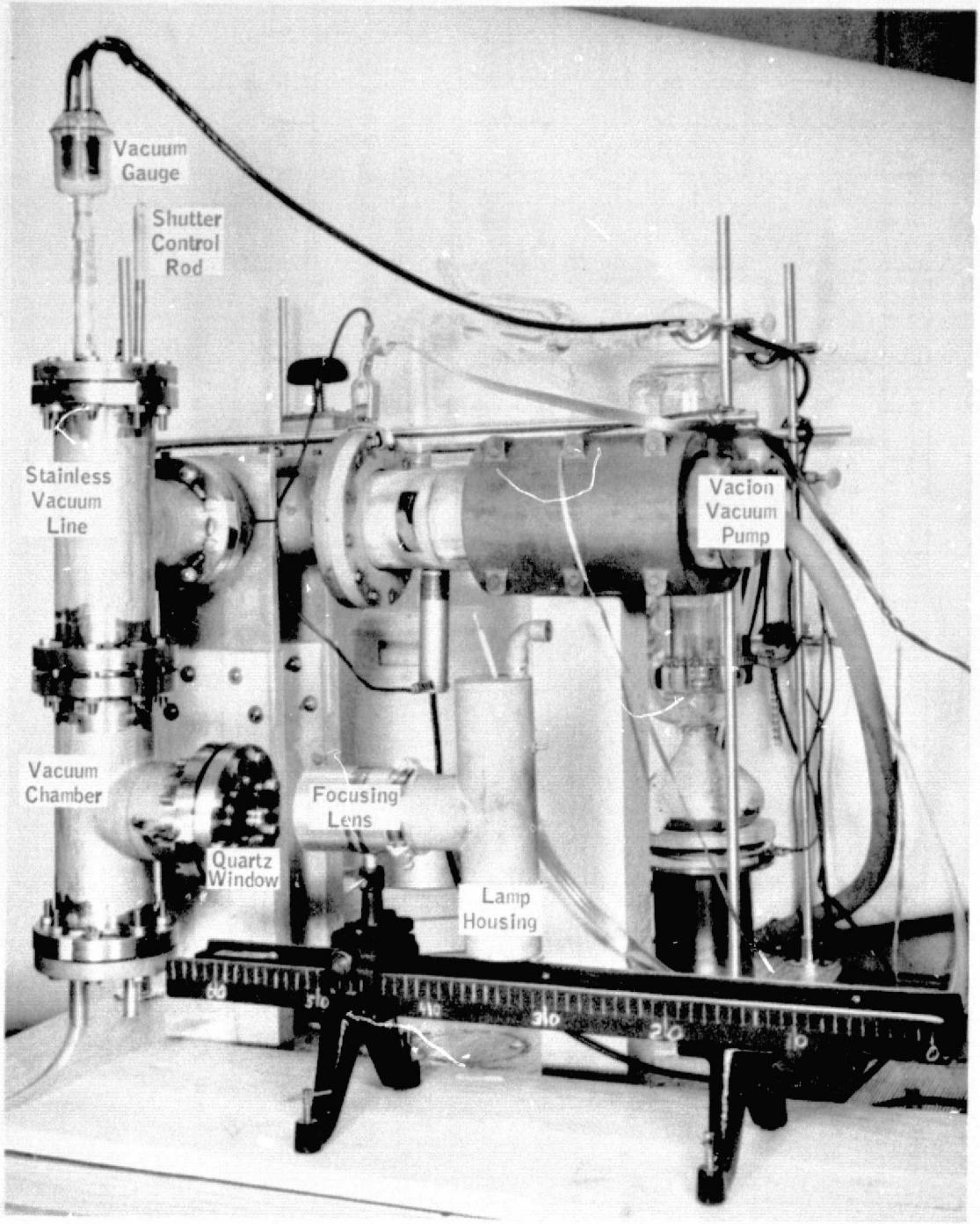

Figure 13 APPARATUS FOR MEASURING $a/$
62-9665

Another source of error arises from temperature differences within the Hohlraum. The magnitude of this error as a function of wavelength is also shown in figure 12. The example given, for a 5.5 °K difference between the mean temperature of the Hohlraum and the reference area within the Hohlraum, indicates only a small error for wavelengths greater than 2μ. Since, for the current measurements, the temperatures within the cavity were monitored at four separate locations including the reference area and maintained within ± 1 °K of each other, errors from this source are considered negligible.

A third source of error is introduced when the specimen exhibits appreciable diffuse reflectance. This can be neglected in the case of highly polished specimens but may be significant in the case of the impacted specimens.

4. Solar Absorptance and Thermal Emittance Measurements

The method used to measure the solar absorptance (α), thermal emittance (ϵ) and the ratio of α/ϵ, between the temperatures of -30 and 200 °C, was similar to the methods used by Butler, et al,[10] Gaumer,[11] and Gordon.[12] It is based on the following considerations: the rate at which the temperature of a surface changes due to the absorption of solar radiation, can be expressed by the following equation:

$$dT_h/dt = \frac{a\alpha I}{mC_p} \tag{5}$$

where

dT_h/dt = rate of temperature change of the surface due to absorption

a = absorbing area

I = intensity of the incident radiation

m = mass of the specimen

C_p = heat capacity of the specimen.

The spacecraft or specimen, while being heated by solar radiation, emits thermal radiation of a different intensity and spectral distribution. The rate of energy loss due to thermal emittance can be expressed by the following:

$$dT_c/dt = \frac{A\epsilon\sigma T^4}{mC_p} \tag{6}$$

where

dT_c/dt = rate of temperature change due to emittance

A = radiating area

σ = Stefan-Boltzmann constant

T = temperature of the specimen.

At equilibrium,

$$dT_h/dt = dT_c/dt$$

or

$$\frac{a\alpha I}{m C_p} = \frac{A\epsilon\sigma T_E^4}{m C_p}$$

and

$$T_E^4 = \frac{\alpha a I}{\epsilon A \sigma} \quad . \tag{7}$$

Thus, the equilibrium temperature (T_E) of a given size specimen exposed to a constant intensity radiation (I), is a function only of the α/ϵ ratio.

For the same wavelength the α/ϵ value is unity in accordance with Kirchoff's law. The ratio of total absorptance to the total emittance, however, can be any value because in general the spectral distribution of the incident radiation is different from that of the emitted radiation. When solar radiation impinges on a solid surface, the absorptance of that surface, in the spectral range of the solar radiation (approximately 6000 °K blackbody radiation), defines the amount of absorbed energy. The energy emitted by the surface, on the other hand, is of a longer wavelength since it originates at a surface much colder than the Sun, but it may total either more or less than the solar energy absorbed at the surface. Values ranging between 0.2 and 14 have been reported for the α/ϵ ratio of various materials.[11]

In practice, one side of the specimen was irradiated by simulated solar radiation from a mercury-xenon lamp, while the opposite side and edges radiated to the blackened, liquid nitrogen cooled walls of an evacuated chamber. By solving equations (5) and (6) for α and ϵ, respectively, it can be seen that α can be obtained from the heating rate, and ϵ from the cooling rate.

$$\alpha = \frac{m C_p}{a I} \, dT_h/dt \tag{8}$$

and

$$\epsilon = \frac{m C_p}{A \sigma (T^4 - T_w^4)} \, dT_c/dt \tag{9}$$

Since all the quantities on the right hand side of the equations can be measured or obtained from the literature, both α and ϵ can be calculated.

Although the ratio α/ϵ can be calculated from the above data, it can also be obtained from the steady state measurement of the equilibrium temperature by the following equation derived from equations (8) and (9).

$$\alpha/\epsilon = \frac{A \sigma (T_E^4 - T_w^4)}{a I} \tag{10}$$

A photograph of the apparatus used for the α/ϵ measurements is shown in figure 13. The specimen, a 0.5-inch diameter disc, 0.06-inch thick, was suspended in the evacuated cylinder in front of the silica window on a chromel-alumel thermocouple.

The hot junction of a 40-gage thermocouple was cemented with a thin layer of conducting Sauereisen cement into a 0.018-inch diameter hole drilled radially into the side of the specimen. The temperature change, as indicated by the thermocouple using an ice bath reference junction, was recorded as a function of time on a strip-chart recorder using a chart speed of 0.5 in./min.

The chamber was evacuated by a pumping system which consisted of a mechanical pump, a three-stage oil diffusion pump and a Vacion pump.

In the early stages of the investigation, a mercury diffusion pump was used. Evidence of an amalgam coating on the gold specimen indicated that a cleaner vacuum was necessary. The mercury diffusion pump was, therefore, replaced by the oil diffusion pump and the Vacion pump was incorporated into the system. The Vacion pump eliminated the need for the diffusion and mechanical pumps during the measurements as they were only required to reduce the initial pressure to below 10^{-4} mm Hg. After reaching this vacuum, both the diffusion and mechanical pumps were turned off and the vacuum was maintained and improved solely by the Vacion pump. The measurements were made at pressures of less than 10^{-7} mm Hg. This vacuum was deemed sufficient for the measurements; Butler and Inn,[13] as well as Gordon[12] found that at pressures less than 10^{-4} mm Hg, any effect of conduction through the gas was negligible.

The radiation source was a Hanovia 1000-watt xenon-filled mercury arc lamp. The spectral distribution of its radiation is approximately that of the solar spectrum, although considerably richer in ultraviolet radiation. The lamp was mounted on an optical bench in front of the window of the specimen chamber. The intensity of the radiation incident on the specimen was controlled by varying the position of the lamp along the optical bench. The radiant flux incident on the specimen for various positions of the source was evaluated by irradiating a blackened (Parson's Black, $\epsilon = 0.985$) copper calorimeter disc, the same size as the specimen mounted inside the vacuum chamber. The flux, I , was calculated using the following equation:

$$I = \frac{m\, C_p\, dT/dt}{\alpha a} \qquad (11)$$

where:

m = mass of the calorimeter

C_p = specific heat of copper

dT/dt = heating rate

a = the irradiated area

α = absorptance of the black surface (0.985).

I includes the simulated solar radiation from the lamp as well as a correction factor because of stray or reflected radiation from the walls and window of the chamber.

To be able to determine the incident flux on the specimen at the time when the equilibrium temperature is achieved, a correlation between the incident flux and the output of an external thermopile was measured. The results of several runs to establish this correlation, and to later substantiate it, are given in figure 14. For each run, the external thermopile output reading (mv) was taken when the specimen had reached equilibrium temperature. The incident flux at that time was then obtained from the correlation curve. The data from several runs to establish this correlation indicate a precision of better than ±5 percent.

To investigate the effect of variations in line voltage on the output of the mercury-xenon lamp, the voltage to the lamp was varied by means of a slide wire resistor. The α/ϵ for an impacted platinum specimen was determined with the lamp at a given distance from the specimen, but at three different line voltages. For each voltage, a different flux, as measured by the external thermopile, as well as a different equilibrium temperature, was recorded. The measured α/ϵ, however, was constant. The results of the three determinations follow:

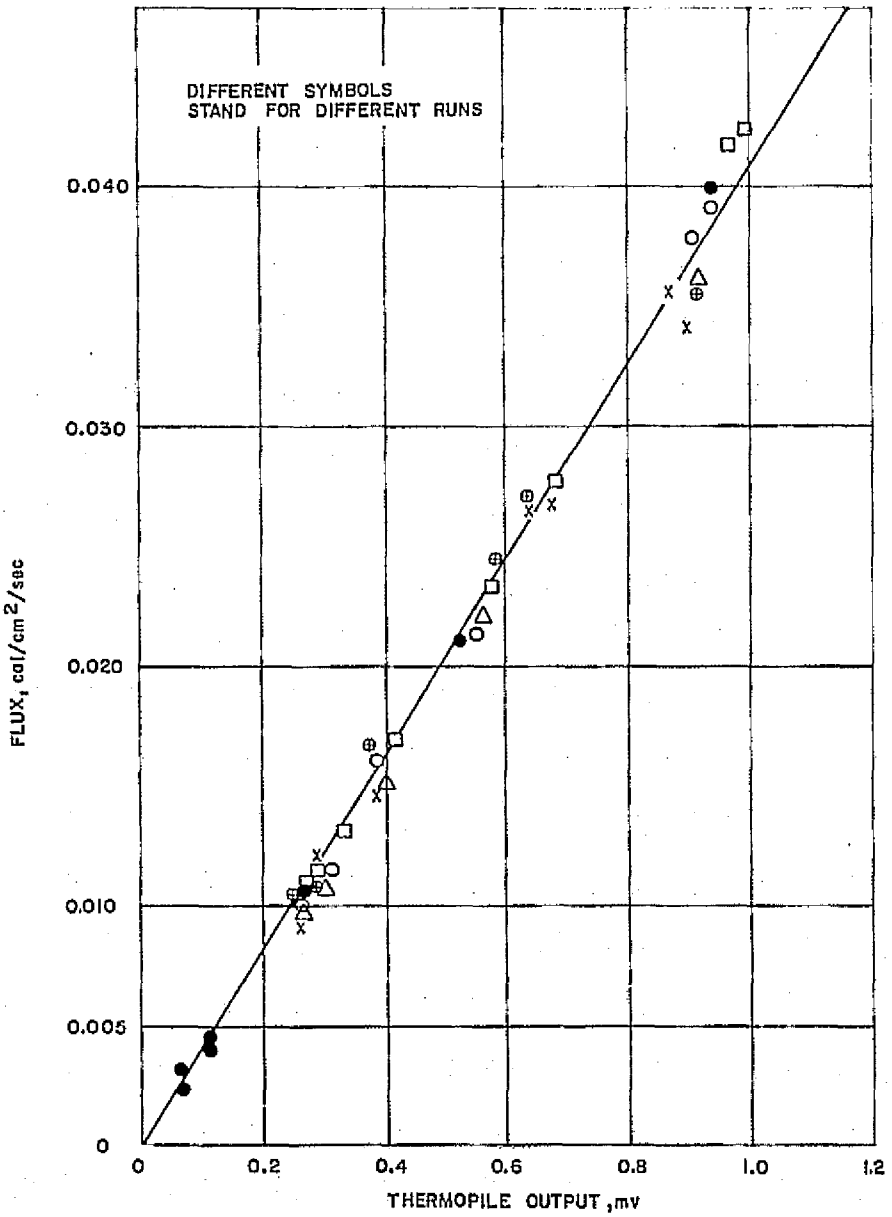

63-8012

Figure 14 CORRELATION BETWEEN INCIDENT FLUX AND EXTERNAL THERMOPILE OUTPUT

Line Voltage	Thermopile Reading (mv)	Flux ($cal/cm^2/sec$)	Equilibrium Temperature (°C)	α/ϵ
106.2	0.379	0.0155	51	2.25
109.7	0.413	0.0170	58	2.24
112.2	0.451	0.0185	65	2.24

From these data, it was concluded that line voltage variations resulted in corresponding variations in the radiant flux and specimen temperature. By nearly simultaneous measurements of the flux and temperature, however, the results of the α/ϵ measurements were not affected. Since such measurements are possible only under steady state conditions, α/ϵ values obtained by the temperature equilibrium method were considered to be more reliable than values calculated from rate measurements.

II. RESULTS AND ANALYSIS

The results of the surface characterization measurements showing the number of craters in each specimen, their average diameter and depth, their depth to diameter ratio, and total area damaged are shown in table I. The distribution of the diameters of the craters are given in figures 15 through 31.

The wide distribution of crater sizes, particularly the large number of craters smaller than 50 μ, in the light gas gun exposures, was apparently caused by the presence of foreign particles in the gas stream. These foreign particles are shown in the strip films as a cloud of fine particles traveling at somewhat slower velocities behind the initial wave of tungsten particles. The presence of such foreign particles in the gas stream was substantiated by a test firing into a tube of silicone grease. A photomicrograph of the grease showed the presence of a large number of particles smaller than 20 μ. Although the impingement of foreign particles on the specimen makes analysis based on ballistic theory difficult, it had the effect of a better simulation of the micrometeorite dust encountered in space and resulted in impacted surfaces more like those expected from the bombardment by particles of different shapes and sizes.

An apparent anomaly exists in the fact that the average dimensions of the craters resulting from the low velocity (5000 ft/sec (1500 m/sec)) impacts are larger than those resulting from the high velocity impacts. This is undoubtedly due to the large number of small foreign particles present in the light gas gun exposures which resulted in a prevalence of small craters that effectively lowered the average dimensions. The composite photographs (figures 32 to 35) showing the specimens after impact by both high (20,000 ft/sec (7000 m/sec)) and low (5000 ft/sec (1500 m/sec)) velocity microprojectiles, are more illustrative of the effect of the velocity and/or density of the impinging particle than is a comparison of the average dimensions of the craters.

Part A of each photograph represents the surface of the sample impacted by Zircaloy particles traveling with an average velocity of 5000 ft/sec (1500 m/sec). The portion marked with B represents metal surfaces damaged by tungsten particles of 20,000 ft/sec (7000 m/sec) velocity. On all metal samples investigated, the damage done by impacting at the lower velocity shows fewer number, smaller diameter craters than is the case with samples impacted at the high velocity. In addition, the rims of the craters protrude much more from the surfaces damaged by the high velocity particles. It is obvious that these visually observable surface differences cause marked changes in such optical properties as reflectance, solar absorptance, and thermal emittance.

The effect of the momentum of the impinging projectiles is also evident in the graphs of the distribution of crater sizes (figures 15 to 31). In the cases of high velocity impacts (20,000 ft/sec (7000 m/sec)) craters as large as 900 μ were measured whereas in the cases of low velocity (5000 ft/sec (1500 m/sec)) the largest craters measured where less than 350 μ in diameter.

TABLE I

DESCRIPTION OF DAMAGE TO SPECIMENS

Material		Projectile Velocity (ft/sec)	Projectile Velocity (m/sec)	Number of Craters	Average Diameter (microns)	Average Depth (microns)	Depth Diameter (microns)	Area Damage (percent)	Knoop Hardness 100-g load
Al	R	5,000	1500	549	123	289	2.35	3.41	22
Al	R	20,000	7000	7,830	54	183	3.39	18.9	
Al	a/ϵ	20,000	7000	19,467	27	78	2.87	17.6	
Au	R	5,000	1500	630	213	241	1.13	9.99	40
Au	R	17,000	5200	5,526	63	61	0.97	21.47	
Au	a/ϵ	20,000	7000	8,380*	53	60	1.13	29.68	
SS 304	R	5,000	1500	327	111	172	1.55	1.42	219
SS 304	R	20,000	7000	3,672	106	179	1.69	17.44	
SS 304	a/ϵ	20,000	7000	6,012	74	124	1.68	19.04	
Cr	R	5,000	1500	663	130	196	1.51	3.88	697
Cr	R	20,000	7000	3,321	125	239	1.91	21.10	
Cr	a/ϵ	20,000	7000	1,764*	112	237	2.12	11.40	
Pt	R	20,000	7000	2,844	182	189	1.04	38.20	120
Pt	a/ϵ	20,000	7000	4,099*	122	127	1.04	34.24	
SS 316	R	5,000	1500	438	205	186	0.91	6.43	
W	R	5,000	1500	456	120			2.27	
Ag	R	5,000	1500	710	175	306	1.75	7.61	

*Total number of craters on both sides of a/ϵ specimens.

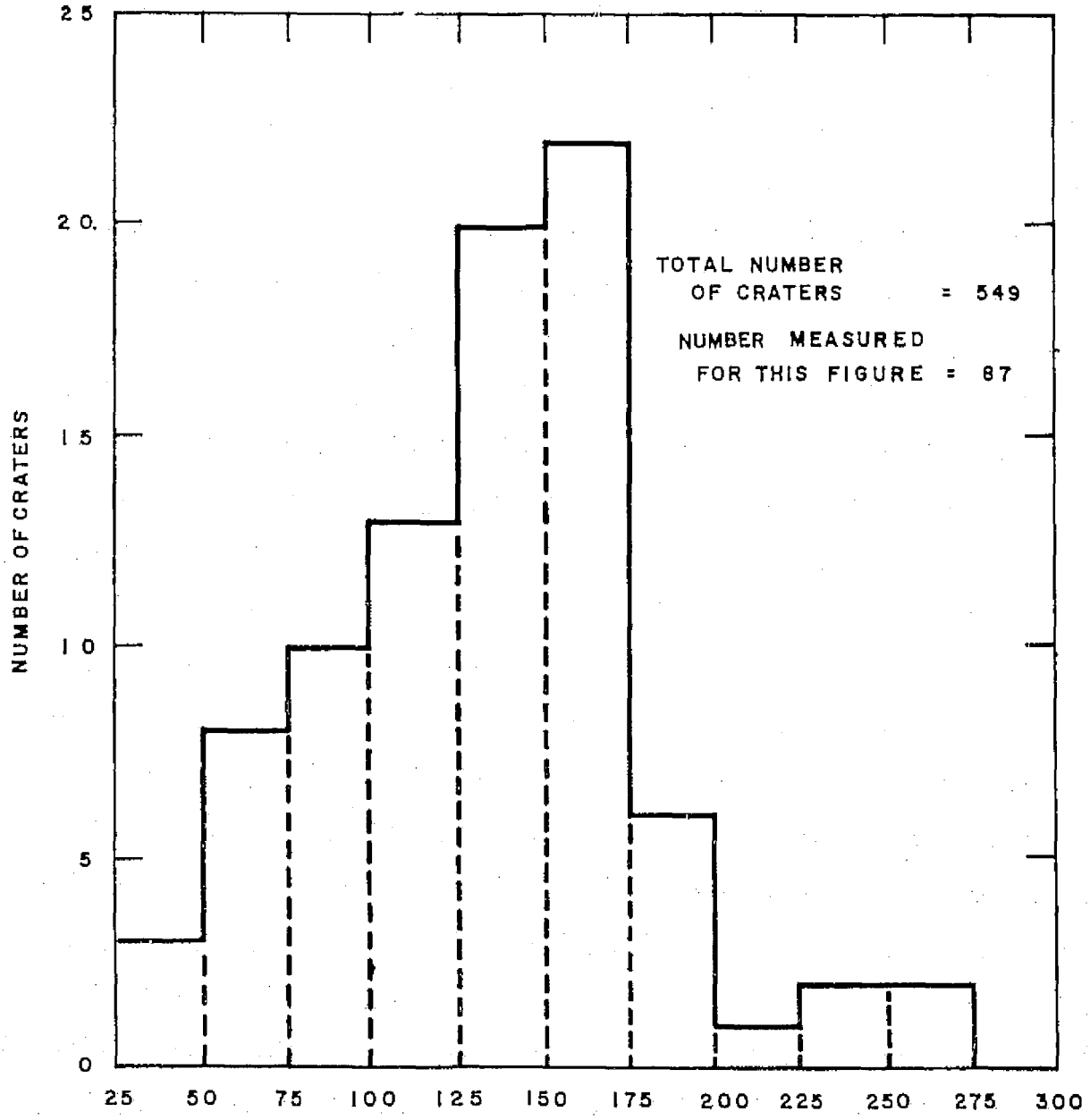

Figure 15 DISTRIBUTION OF CRATER DIAMETERS IN IMPACTED ALUMINUM (SHOT 53)--
REFLECTANCE SPECIMEN, 5000 FT/SEC (1500 M/SEC) PROJECTILES
62-6173

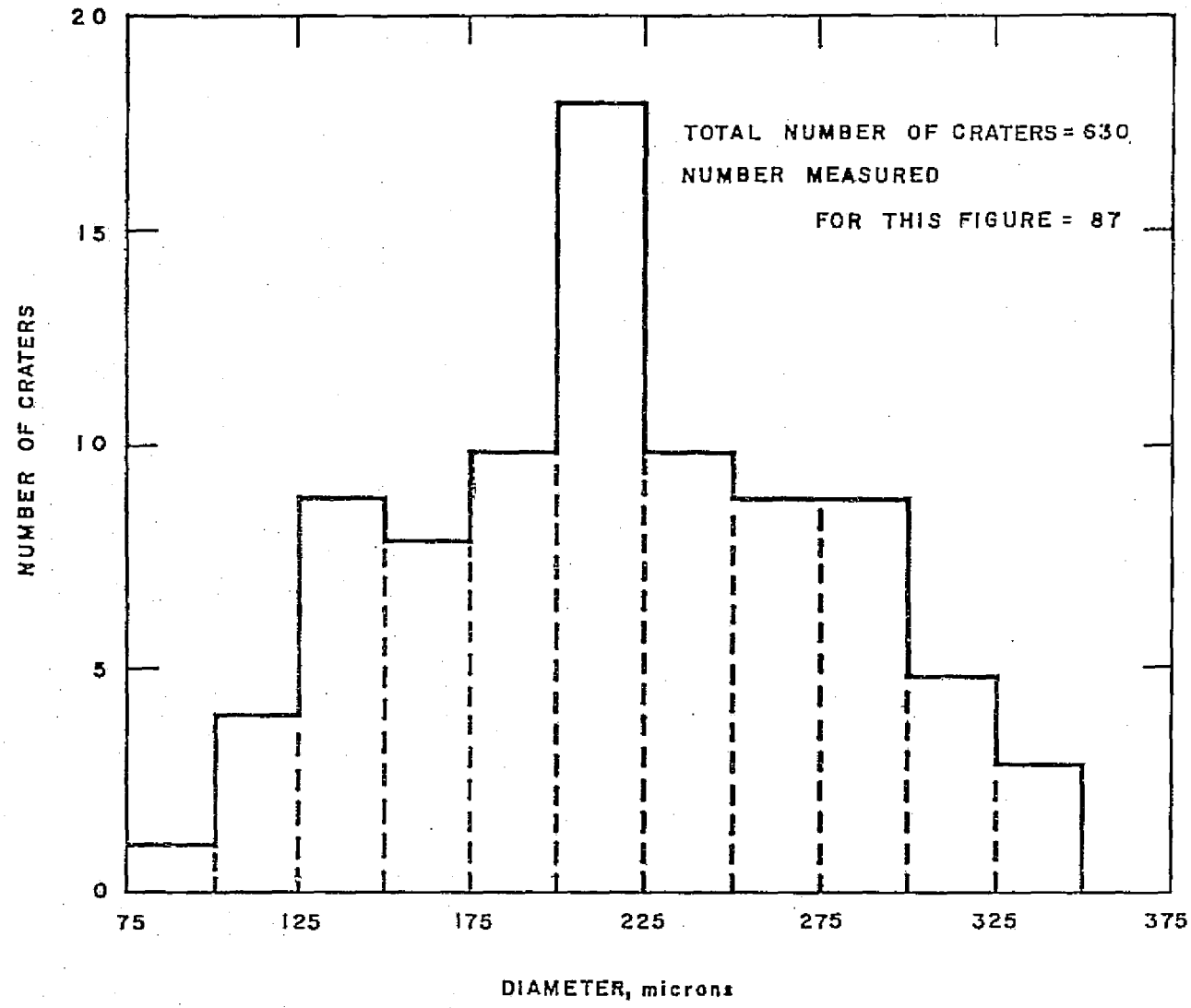

Figure 16 DISTRIBUTION OF CRATER DIAMETERS IN IMPACTED GOLD (SHOT 67)--
REFLECTANCE SPECIMEN, 5000 FT/SEC (1500 M/SEC) PROJECTILES
62-6170

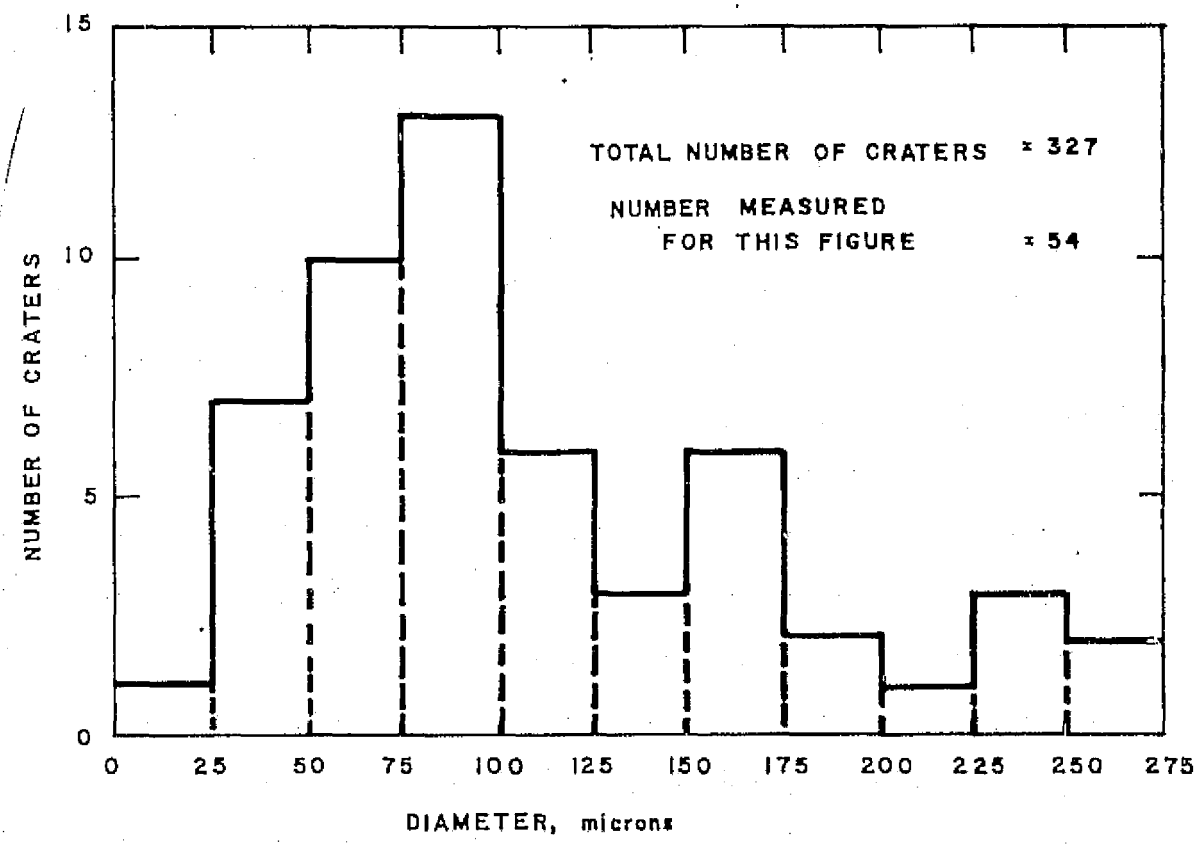

Figure 17 DISTRIBUTION OF CRATER DIAMETERS IN IMPACTED STAINLESS STEEL, TYPE 304 (SHOT 46)--REFLECTANCE SPECIMEN, 5000 FT/SEC (1500 M/SEC) PROJECTILES
62-6176

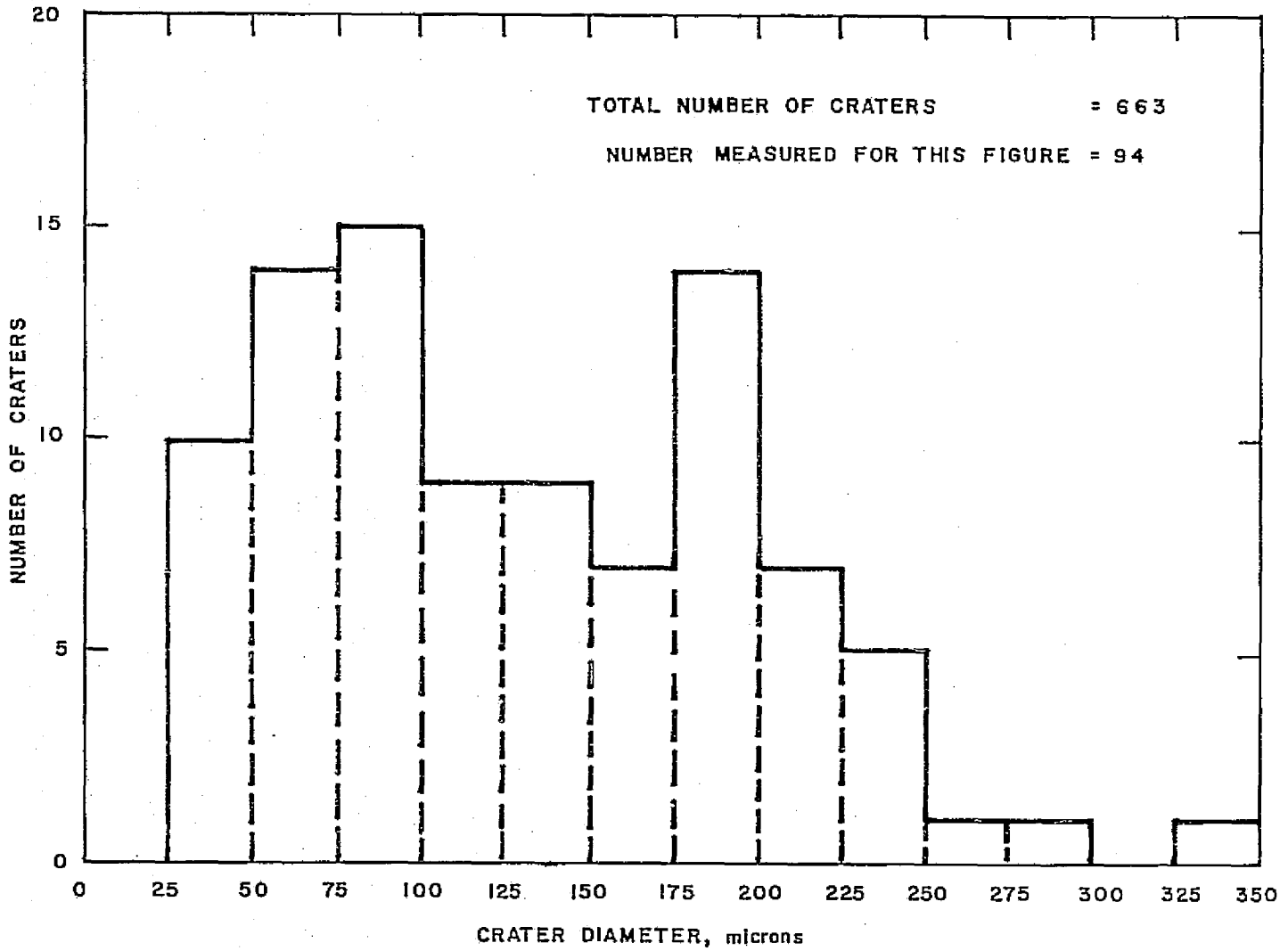

Figure 18 DISTRIBUTION OF CRATER DIAMETERS IN IMPACTED CHROMIUM PLATE (SHOT 54)--REFLECTANCE SPECIMEN, 5000 FT/SEC (1500 M/SEC) PROJECTILES
62-6182

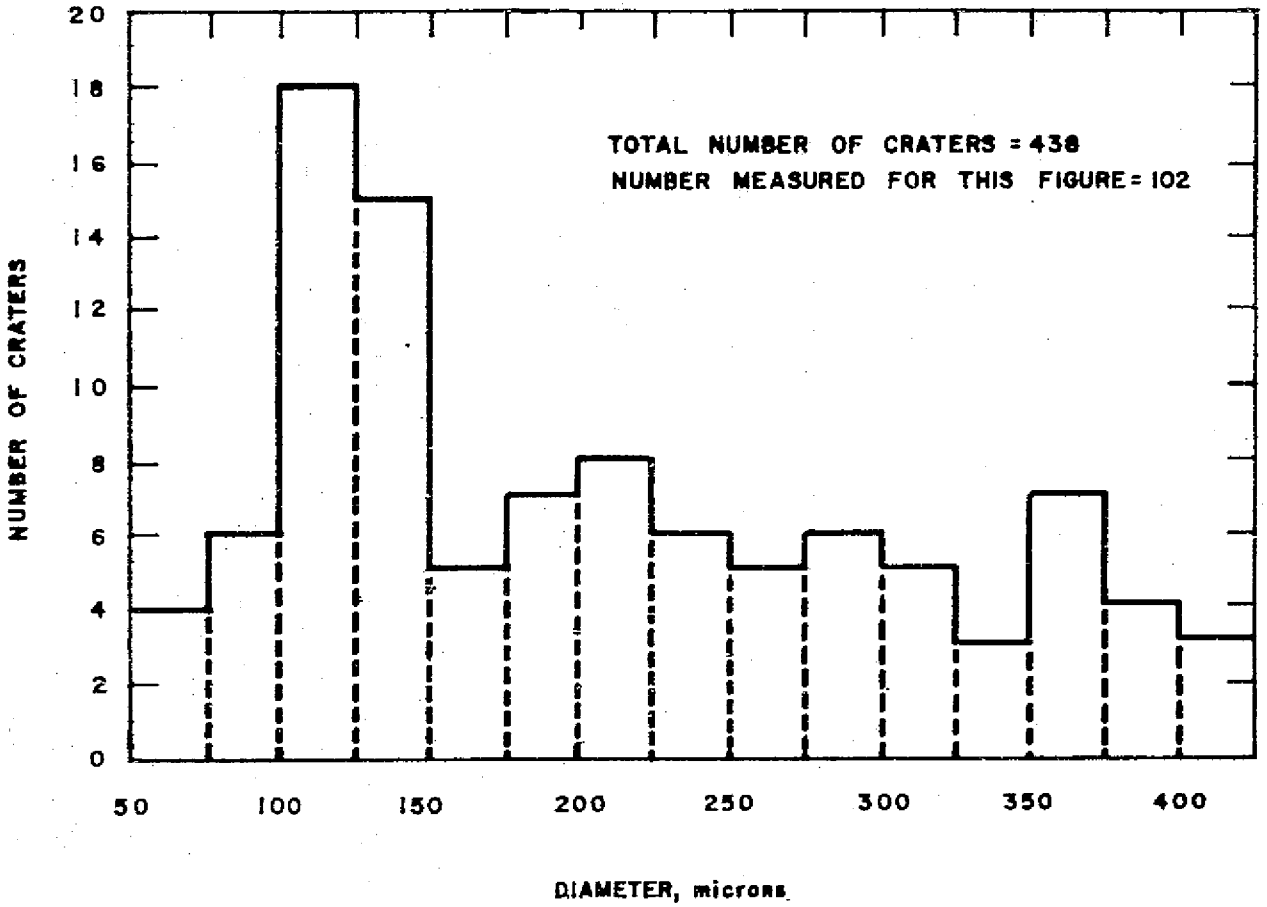

Figure 19 DISTRIBUTION OF CRATER DIAMETERS IN IMPACTED STAINLESS STEEL, TYPE 316 (SHOT 47)--REFLECTANCE SPECIMEN, 5000 FT/SEC (1500 M/SEC) PROJECTILES
62-6179

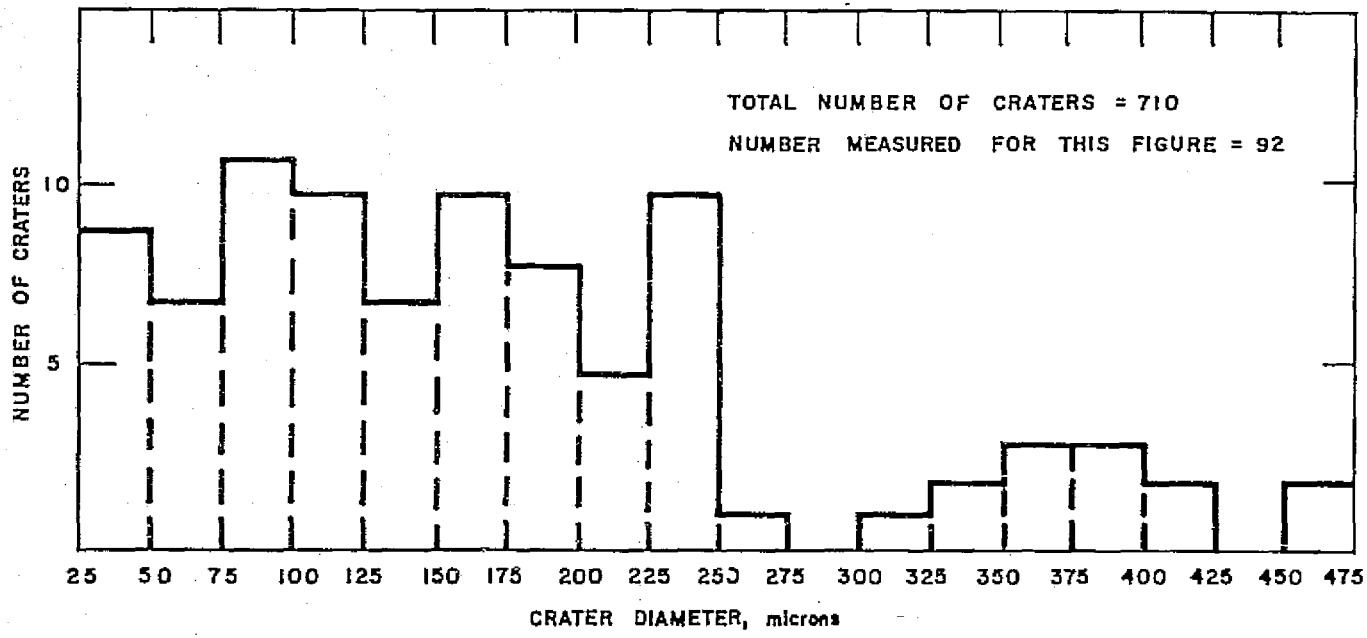

Figure 20 DISTRIBUTION OF CRATER DIAMETERS IN IMPACTED SILVER (SHOT 68)--
REFLECTANCE SPECIMEN, 5000 FT/SEC (1500 M/SEC) PROJECTILES
62-6188

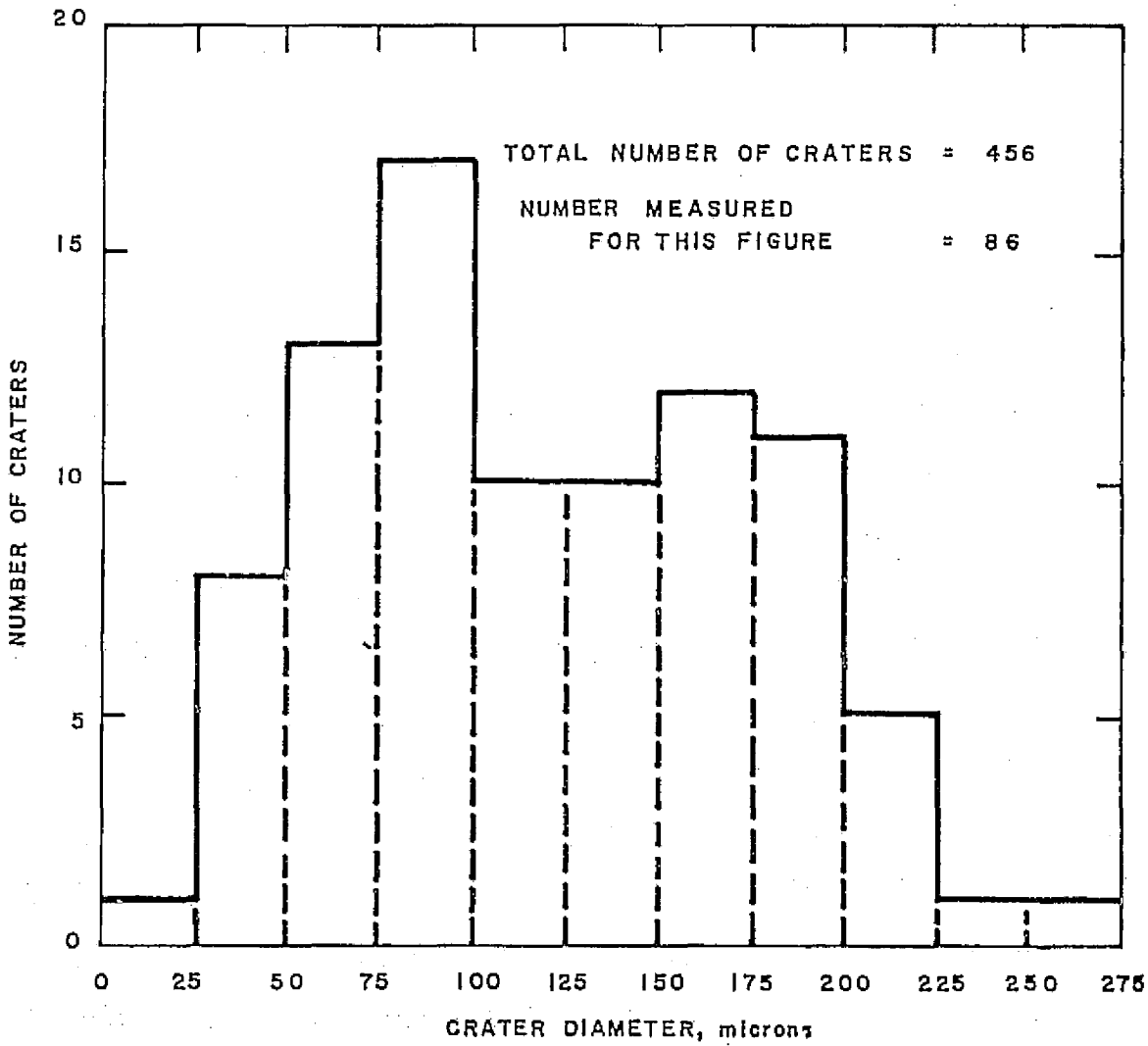

Figure 21 DISTRIBUTION OF CRATER DIAMETERS IN IMPACTED TUNGSTEN (SHOTS 65 AND 66)-- REFLECTANCESPECIMEN, 5000 FT/SEC (1500 M/SEC) PROJECTILES
62-6185

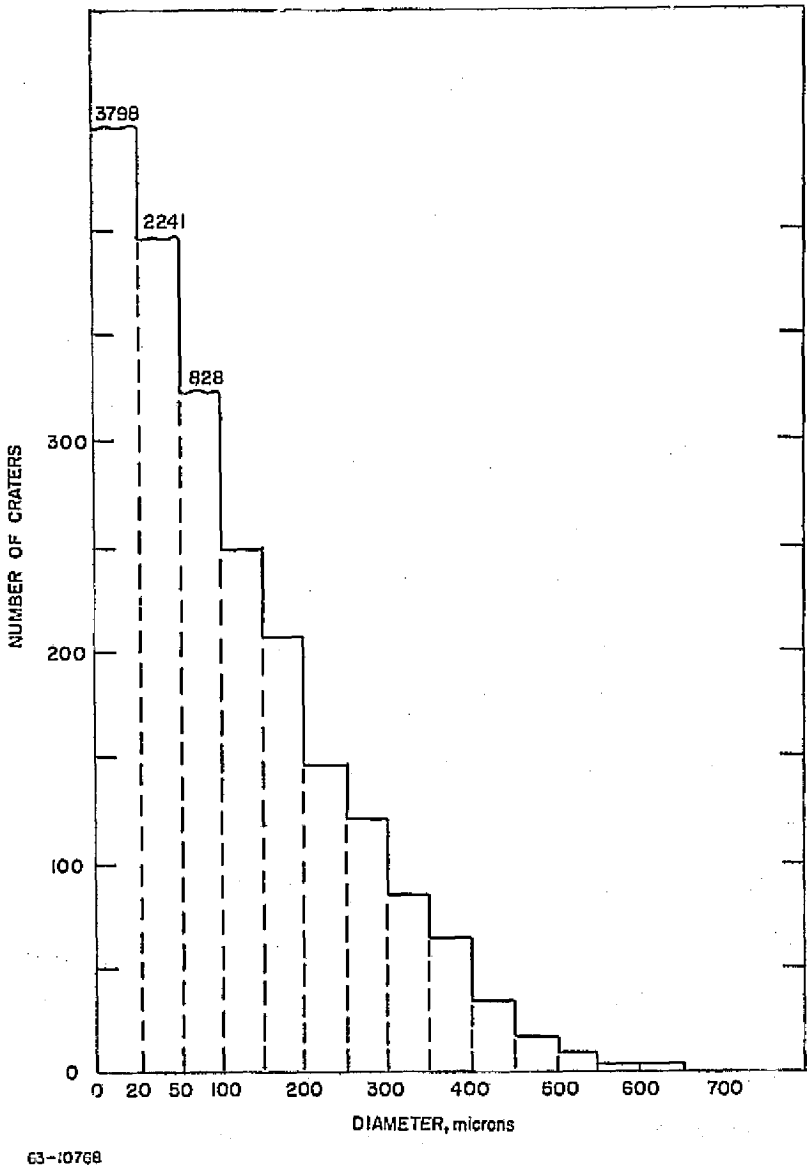

63-10768

Figure 22 DISTRIBUTION OF CRATER SIZES IN IMPACTED ALUMINUM--REFLECTANCE SPECIMEN, 20,000 FT/SEC (7000 M/SEC) PROJECTILES

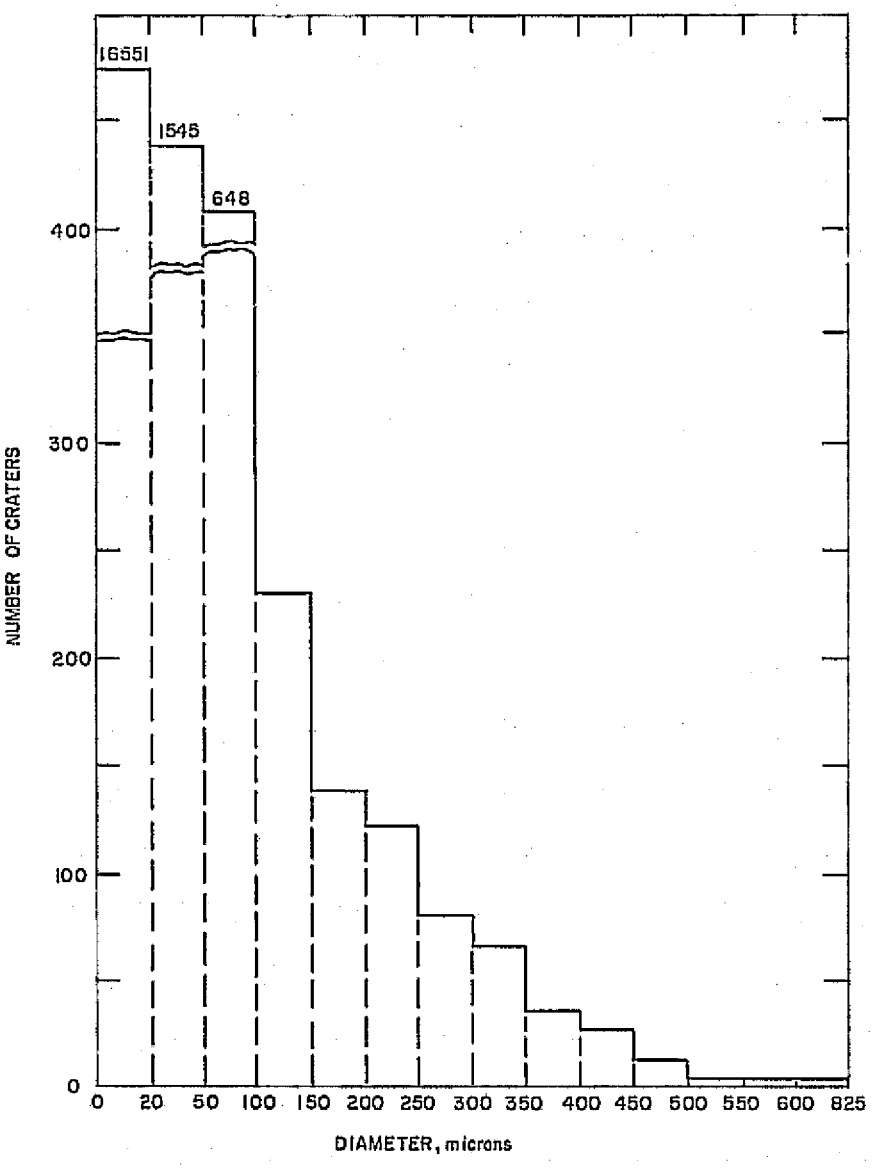

63-10869

Figure 23 DISTRIBUTION OF CRATER SIZES IN IMPACTED ALUMINUM SPECIMEN, 20,000 FT/SEC (7000 M/SEC) PROJECTILES

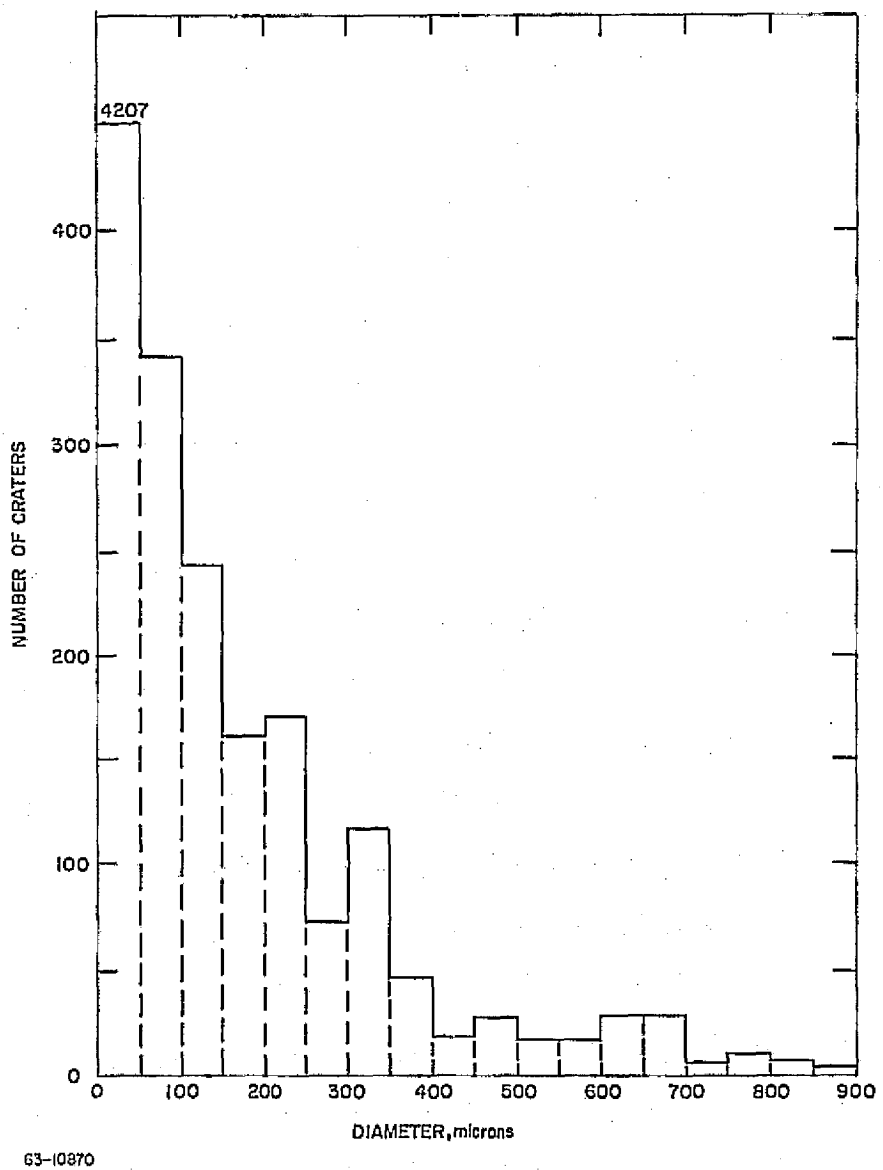

Figure 24 DISTRIBUTION OF CRATER SIZES IN IMPACTED GOLD-- REFLECTANCE SPECIMEN, 17,000 FT/SEC (5200 M/SEC) PROJECTILES

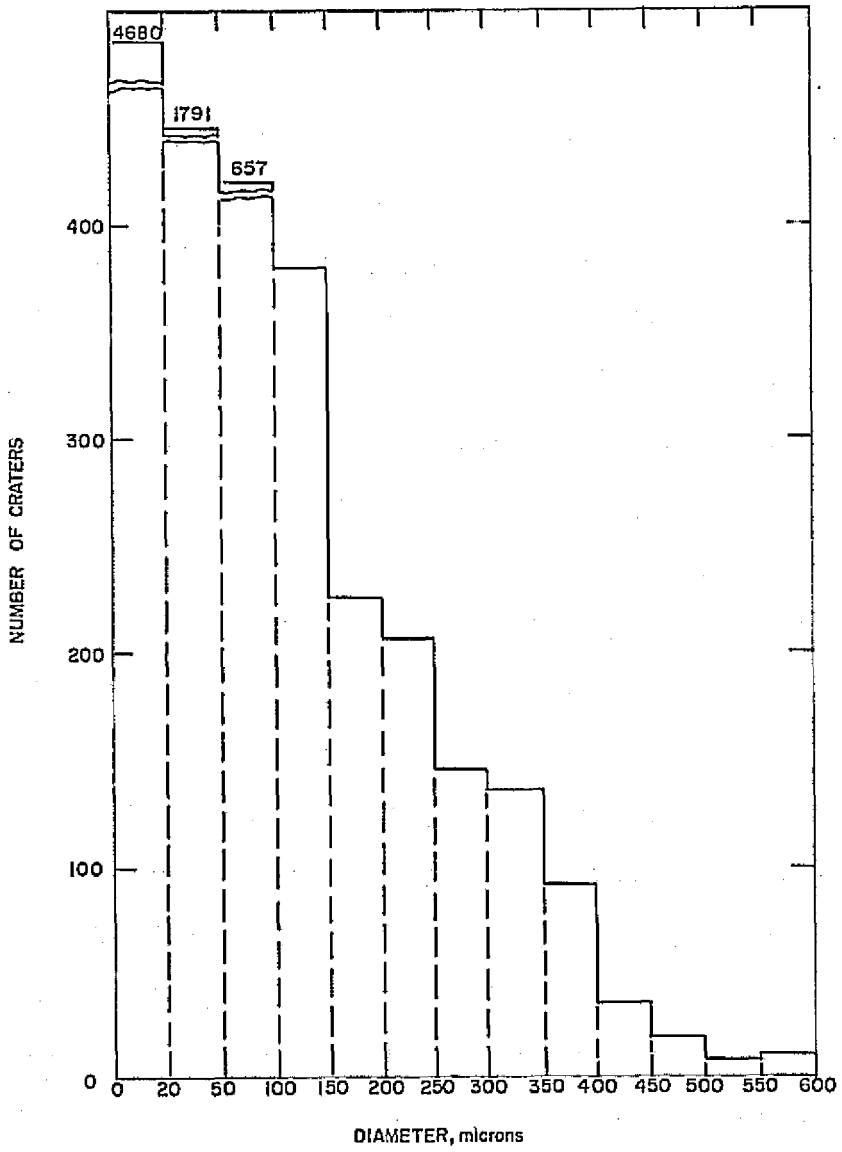

63-10871

Figure 25 DISTRIBUTION OF CRATER SIZES IN IMPACTED GOLD--n/k SPECIMEN, 20,000 FT/SEC (7000 M/SEC) PROJECTILES

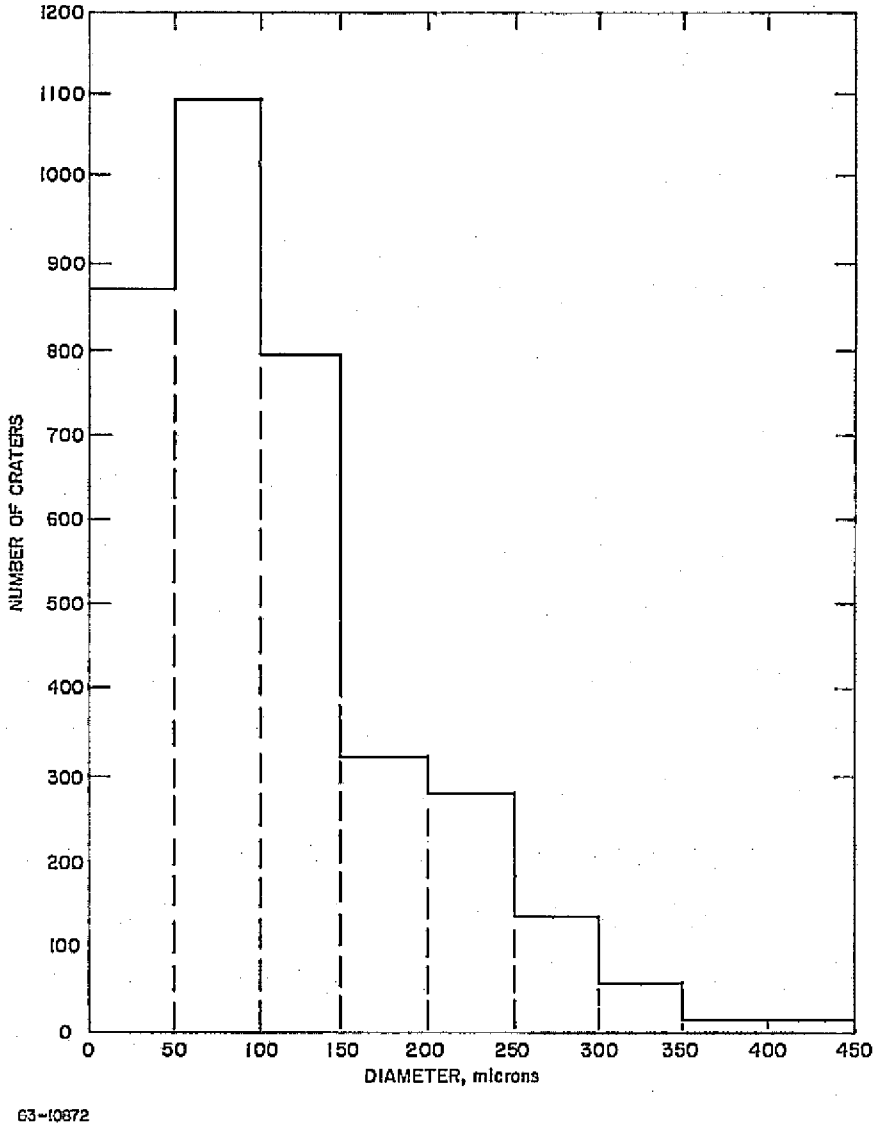

Figure 26 DISTRIBUTION OF CRATER SIZES IN IMPACTED STAINLESS STEEL, TYPE 304--REFLECTANCE SPECIMEN 20,000 FT/SEC (7000 M/SEC) PROJECTILES

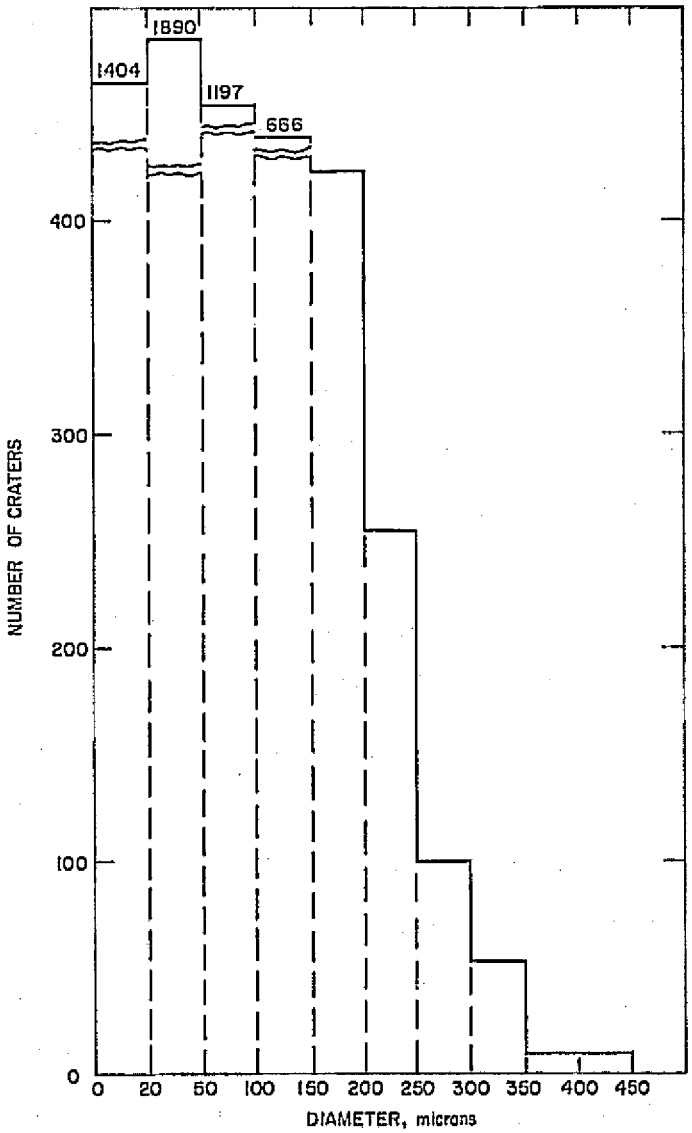

63-10973

Figure 27 DISTRIBUTION OF CRATER SIZES IN IMPACTED STAINLESS STEEL TYPE 304--α SPECIMEN, 20,000 FT/SEC (7000 M/SEC) PROJECTILES

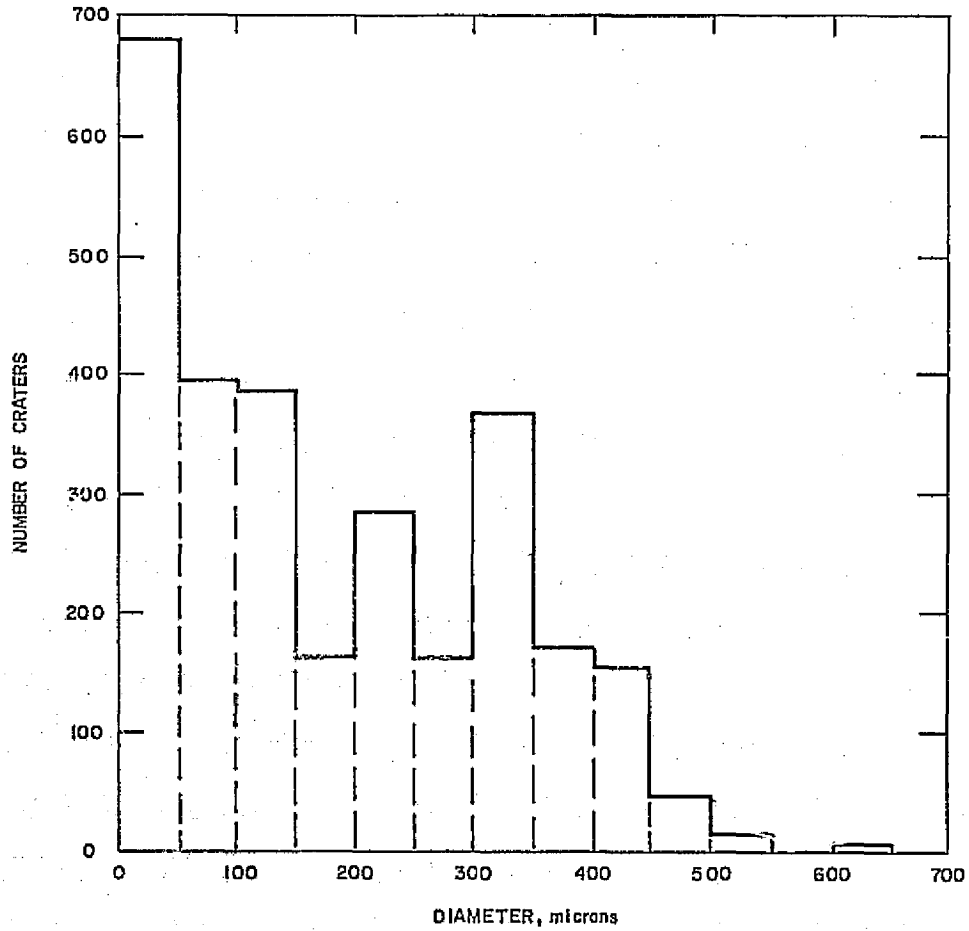

63-10874

Figure 28 DISTRIBUTION OF CRATER SIZES IN IMPACTED PLATINUM--α/ϵ SPECIMEN, 20,000 FT/SEC (7000 M/SEC) PROJECTILES

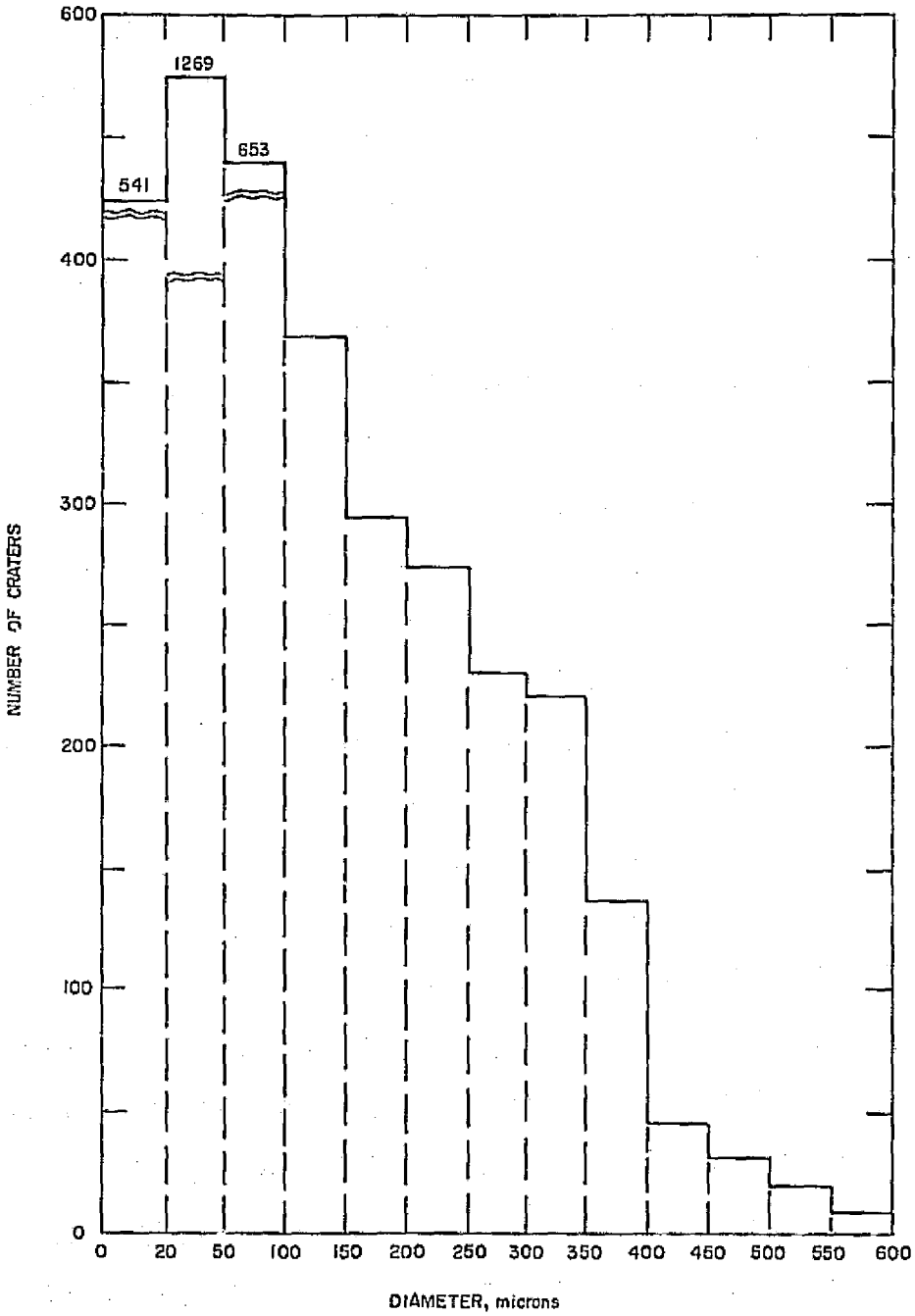

63-10875

Figure 29 DISTRIBUTION OF CRATER SIZES IN IMPACTED PLATINUM--a/ SPECIMEN, 20,000 FT/SEC (7000 M/SEC) PROJECTILES

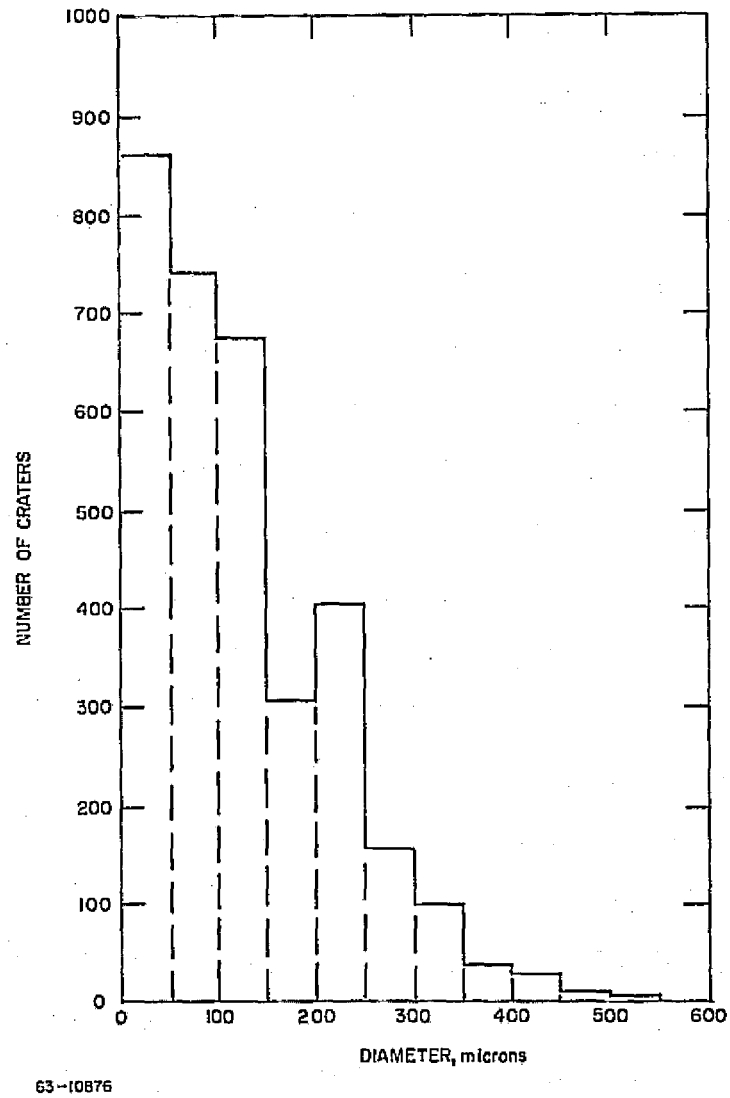

Figure 30 DISTRIBUTION OF CRATER SIZES IN IMPACTED CHROMIUM-PLATED COPPER--REFLECTANCE SPECIMEN, 20,000 FT/SEC (7000 M/SEC) PROJECTILES

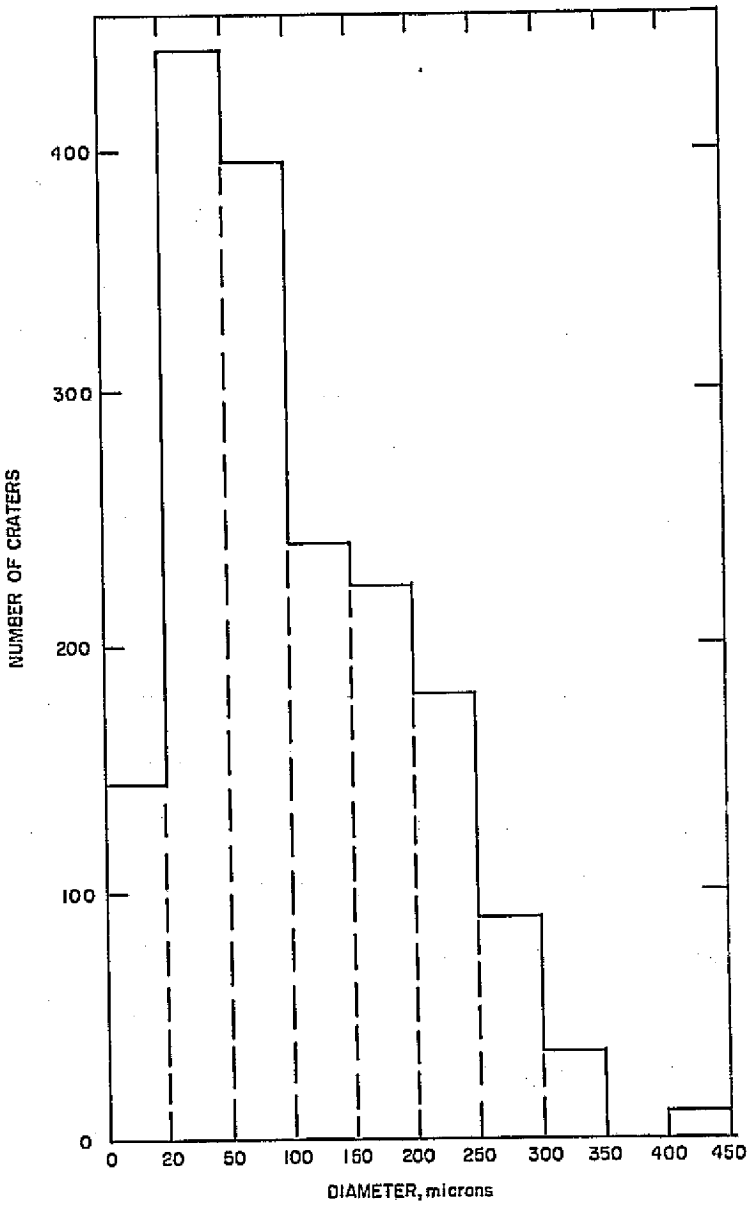

63-10877

Figure 31 DISTRIBUTION OF CRATER SIZES IN IMPACTED CHROMIUM-PLATED COPPER--a/ SPECIMEN, 20,000 FT/SEC (7000 M/SEC) PROJECTILES

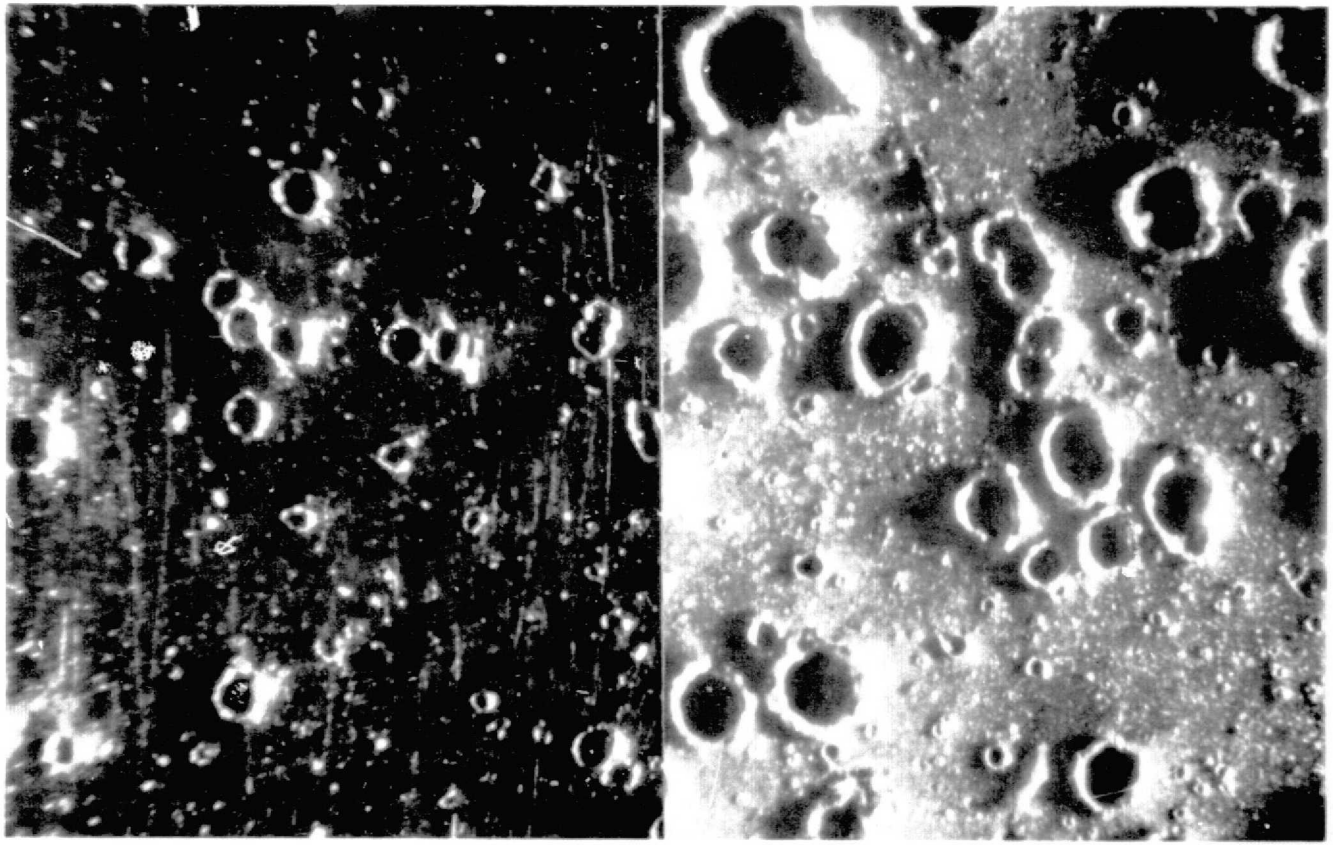

63-10778

Figure 32 COMPOSITE PHOTOGRAPH OF ALUMINUM SPECIMENS DAMAGED BY HIGH AND LOW VELOCITY PROJECTILES; A--5000 FT/SEC (1500 M/SEC), B--20,000 FT/SEC (7000 M/SEC)

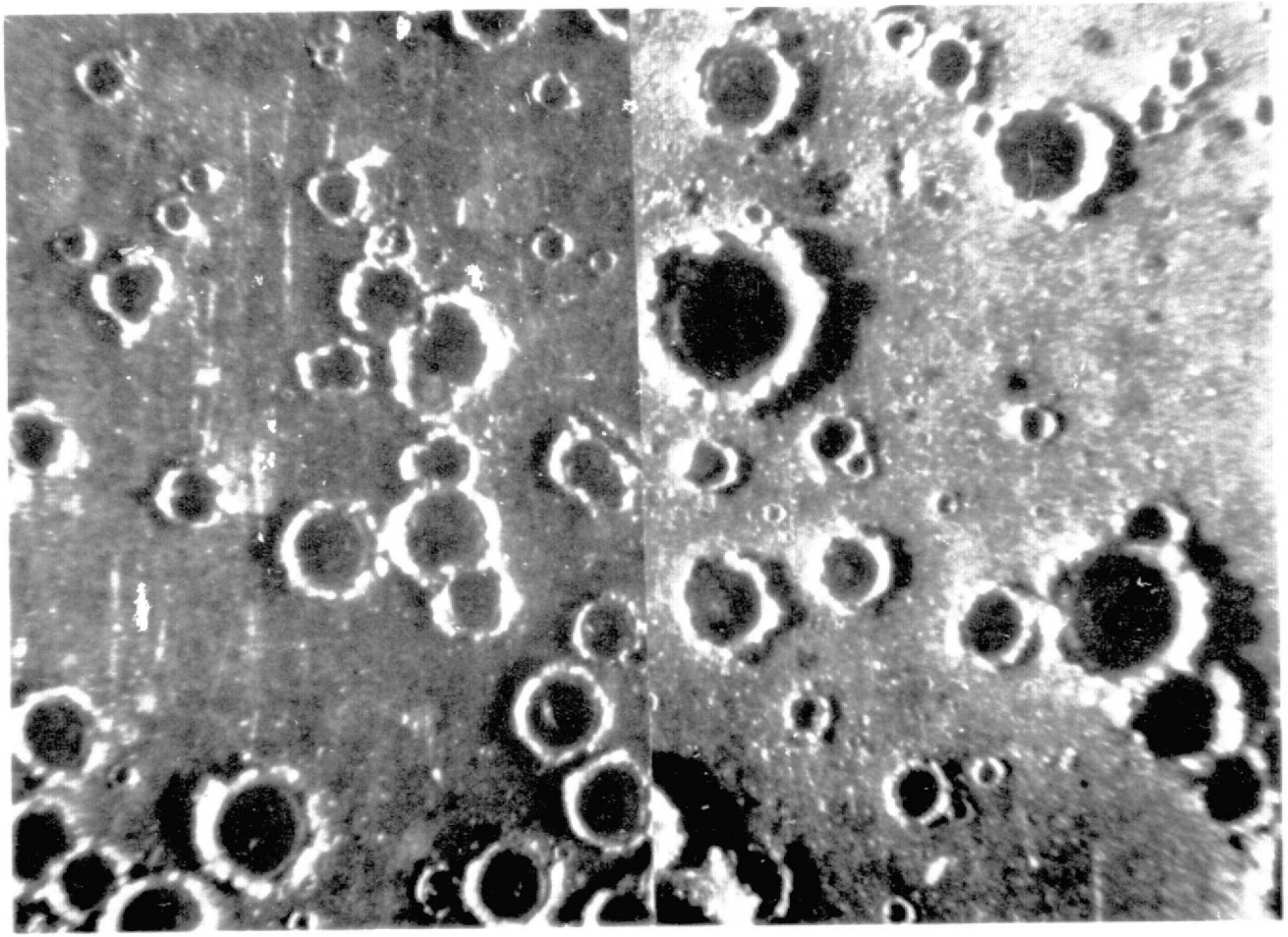

63-10779

Figure 33 COMPOSITE PHOTOGRAPH OF GOLD SPECIMENS DAMAGED BY HIGH AND LOW VELOCITY PROJECTILES; A--5000 FT/SEC (1500 M/SEC), B--20,000 FT/SEC (7000 M/SEC)

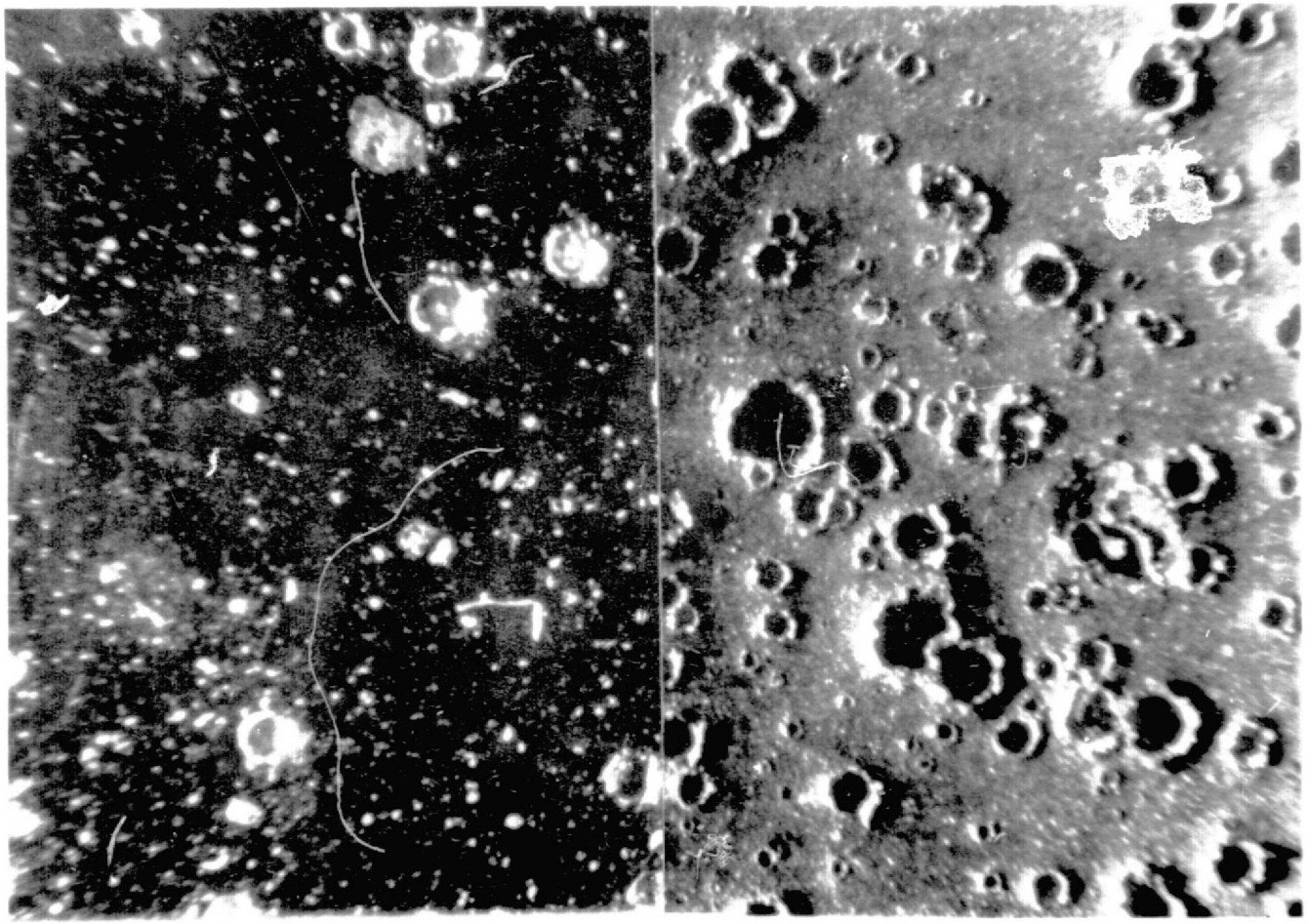

Figure 34 COMPOSITE PHOTOGRAPH OF STAINLESS STEEL 304 SPECIMENS DAMAGED BY HIGH AND LOW VELOCITY PROJECTILES; A--5000 FT/SEC (1500 M/SEC), B--20,000 FT/SEC (7000 M/SEC)

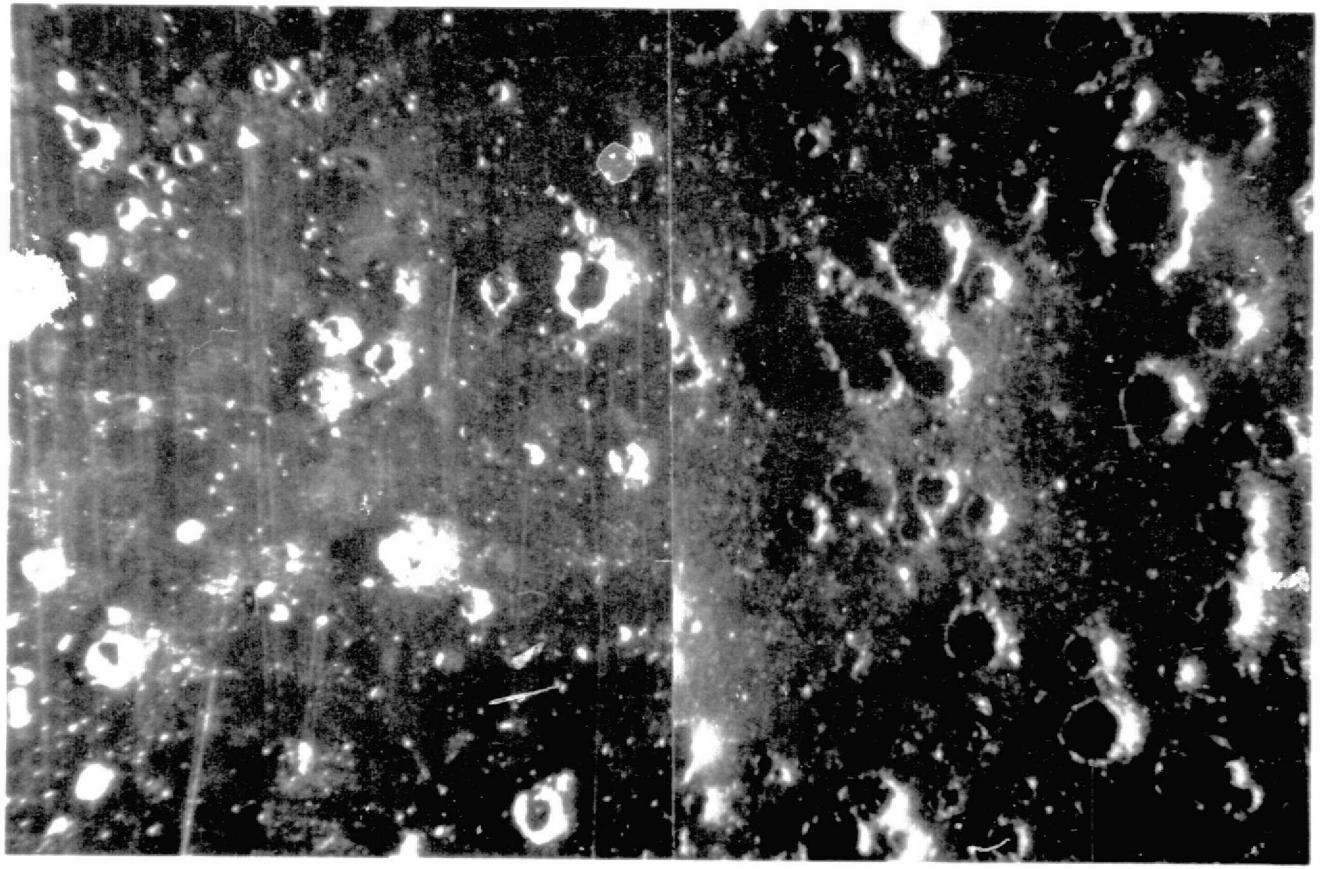

Figure 35 COMPOSITE PHOTOGRAPH OF CHROMIUM-PLATED COPPER SPECIMENS DAMAGED BY HIGH AND LOW VELOCITY PROJECTILES;
A--5000 FT/SEC (1500 M/SEC),
B--20,000 FT/SEC (7000 M/SEC)

Another anomaly is apparent in the relatively large depth-to-diameter ratios observed for the craters of the impacted specimens. Present ballistics theories predict that craters caused by particles traveling at velocities as high as 20,000 ft/sec (7000 m/sec) should have a depth-to-diameter ratio of 0.5. This theory, however, was based on data obtained from impacts of large single projectiles and may not apply to impacts of small particles. This may be particularly true, as in this case, where the impacting particles are the same order of magnitude as the grain size of the target and thus may have a different mechanism of penetration. Similar cases investigated by Gehring[14] showed depth-to-diameter ratios as high as 10:1 where microprojectiles (~40 μ) penetrated a target along a grain boundary. Although no craters with these proportions were found in the present work, it is likely that the same mechanism is responsible for the large depth-to-diameter ratios observed.

The infrared reflectance of the specimens before and after impacting is presented in figures 36 through 43. Data on aluminum, gold, chromium-plated copper, stainless steel 304, and silver are given for specimens impacted by particles traveling at both 5000 and 20,000 ft/sec (1500 and 7000 m/sec), whereas the data on tungsten and stainless steel were obtained only for specimens impacted by 5000 ft/sec (1500 m/sec) particles, and platinum only 20,000 ft/sec (7000 m/sec). In all cases, the infrared reflectance of the impacted specimens was observed to be less than that of the polished specimen.

After exposure to low velocity impacts, the reflectance of the metals was observed to decrease between 1 and 10 percent, whereas after exposure to high velocity impacts, the reflectance was observed to decrease between 10 and 26 percent. The changes in reflectance per crater and per area damaged are given in tables II and III. The differences in the results for the two sets of data must be caused by the differences in the sizes of the craters, since the data have been normalized, as far as number of craters and damaged area are concerned.

The α/ϵ measurements for the metals investigated, before and after impacting by simulated micrometeorites, are given as a function of temperature in figures 44 through 48. These data, obtained from steady state measurements, using equation (10), show that the α/ϵ of all the specimens, with the exception of stainless steel 304, decreased after exposure to the simulated micrometeorite bombardment.

The observed constancy of the α/ϵ ratio for the stainless steel specimen was verified by repeated measurements at several temperatures on both polished and impacted specimens. The results of the four sets of data are given in figure 18. If this apparent insensitivity of the optical properties of stainless steel to microparticle impingement can be substantiated at other levels of surface damage, the advantages of the use of this material as a satellite skin are obvious. It is emphasized, however, that additional experimentation is necessary to verify this conclusion.

TABLE II

REFLECTANCE BEFORE AND AFTER IMPACT BY 5000 FT/SEC (1500 M/SEC) ZIRCALOY PARTICLES

Material	Number of Craters	Area Damaged (percent)	R_o 2 to 24μ (percent)**	R_i 2 to 24μ (percent)**	ΔR (percent)	$\Delta R/R_o$	$\frac{\Delta R/R_o}{A}$	$\frac{\Delta R/R_o}{N}$
Al	549	3.41	97.66	95.81	1.85	1.90	0.557	0.0035
An	630	9.99	97.58	91.49	6.09	6.24	0.625	0.0099
SS 304	327	1.42	87.84	86.11	1.73	1.97	1.387	0.006
Cr *	663	3.88	92.55	89.11	3.44	3.72	0.957	0.0056
SS 316	438	6.43	88.39	85.55	2.84	3.21	0.533	0.0078
W	456	2.27	96.50	92.95	3.55	3.67	1.335	0.0066
Ag	710	7.61	97.93	89.73	6.20	8.37	1.226	0.013

* Chromium-plated copper

**Percent reflectance values obtained by integrating spectral reflectance curves between 2 and 24 μ

TABLE III

REFLECTANCE BEFORE AND AFTER IMPACT
BY 20,000 FT/SEC (7000 M/SEC ZIRCALOY PARTICLES

Material	Number of Craters	Area Damaged (percent)	R_o ** 2 to 24 μ (percent)	R_i ** 2 to 24 μ (percent)	ΔR (percent)	$\Delta R/R_o$	$\frac{\Delta R/R_o}{A}$	$\frac{\Delta R/R_o}{N}$
Al	7830	18.88	97.66	76.17	21.49	22.00	1.17	.0028
Au	5474	21.79	97.58	96.97	10.61	10.87	0.50	.0020
SS 304	3672	17.45	87.84	75.17	12.67	14.42	0.83	.0039
Pt	2844	38.28	94.37	70.10	24.27	25.71	0.67	.0090
*CR	3321	21.08	92.55	76.28	16.27	17.57	0.83	.0053

*Chromium plated Copper
**Percent reflectance values obtained by integrating spectral reflectance curve between 2 and 24 μ.

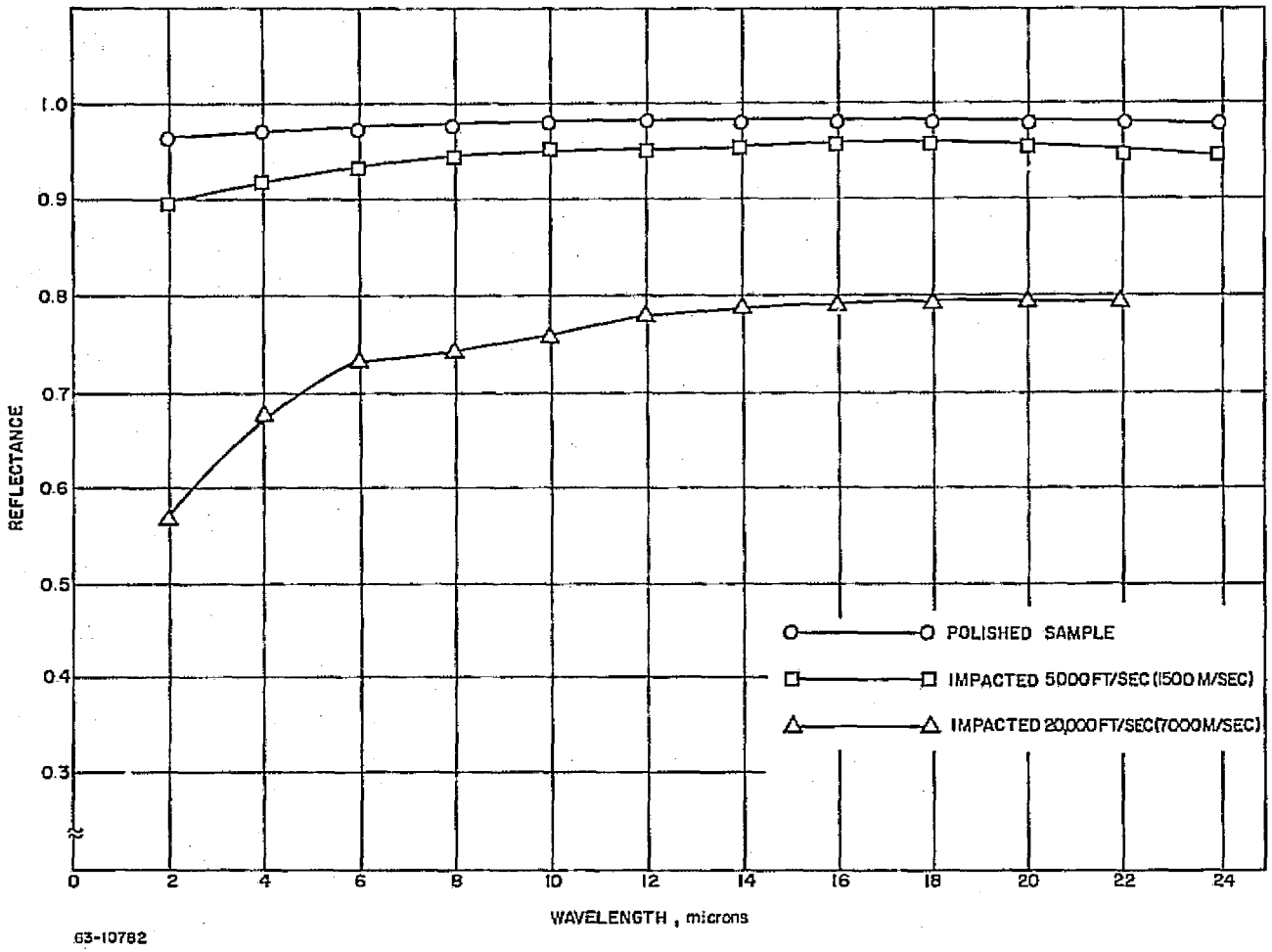

Figure 36 SPECTRAL REFLECTANCE OF ALUMINUM

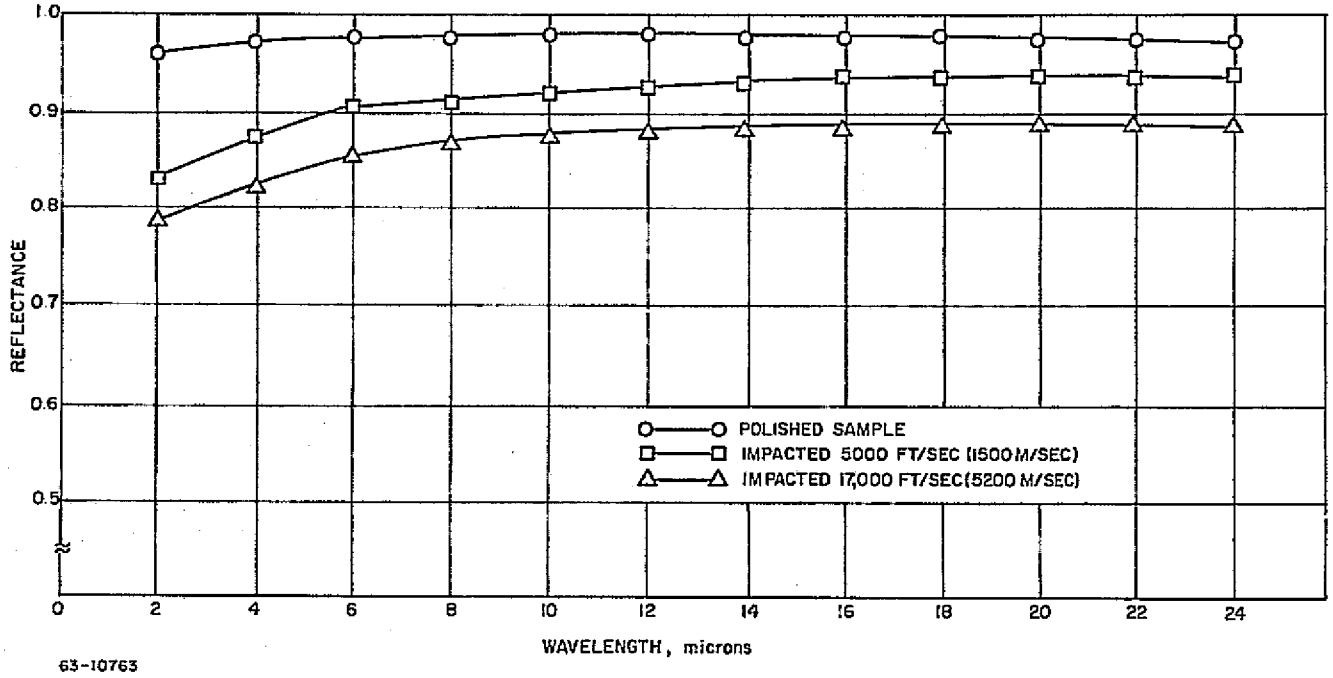

Figure 37 SPECTRAL REFLECTANCE OF GOLD

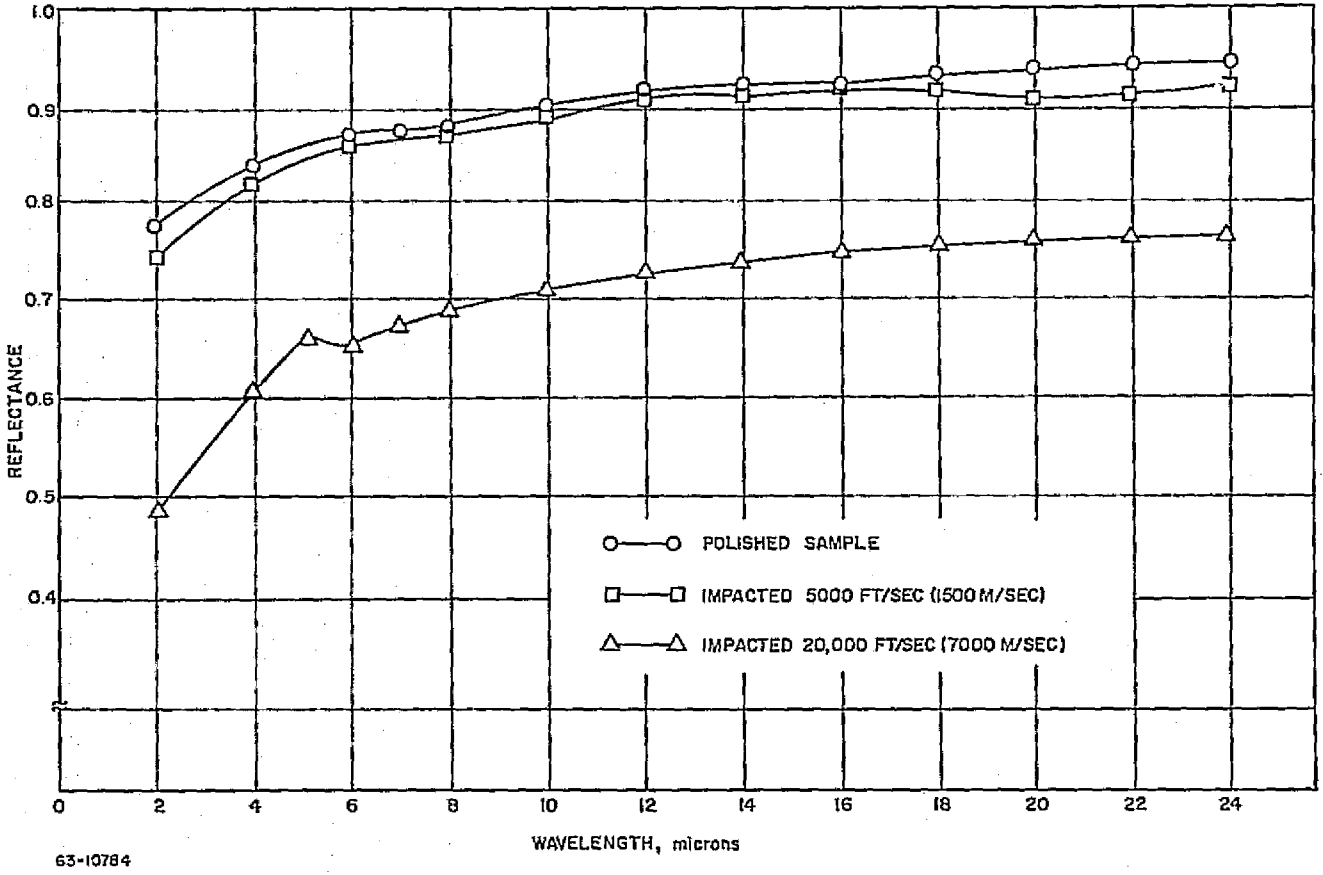

Figure 38 SPECTRAL REFLECTANCE OF STAINLESS STEEL, TYPE 304

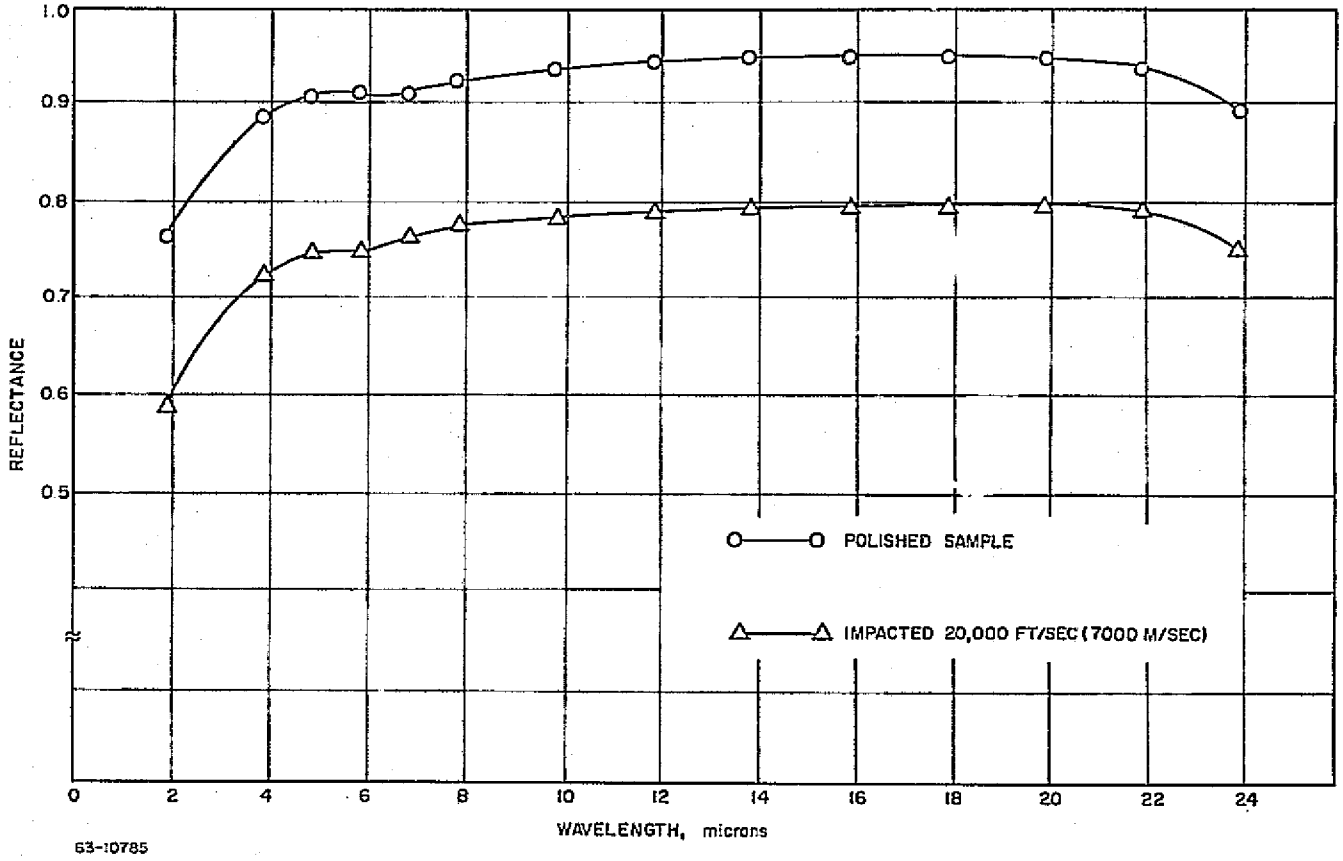

Figure 39 SPECTRAL REFLECTANCE OF PLATINUM

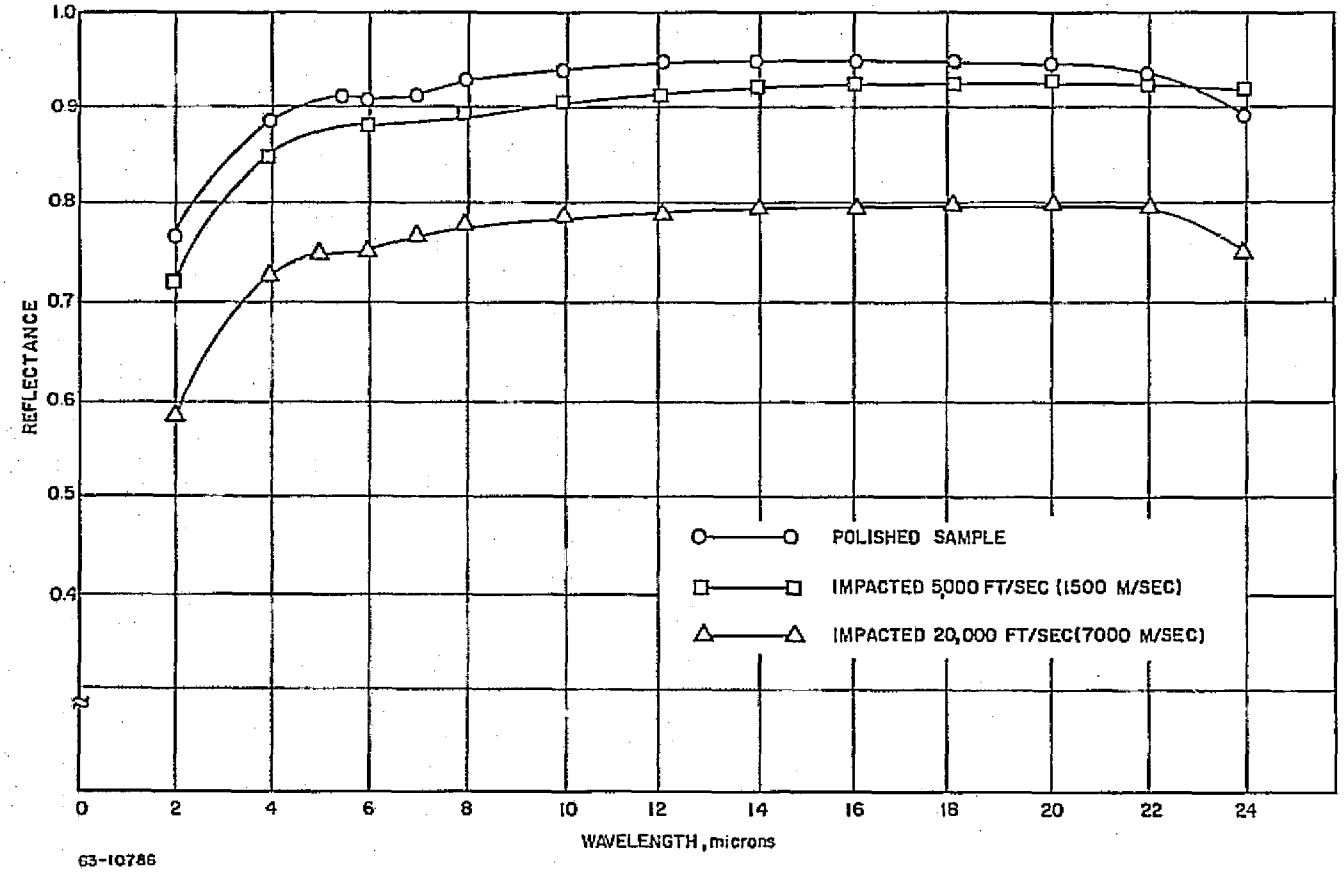

Figure 40 SPECTRAL REFLECTANCE OF CHROMIUM-PLATED COPPER

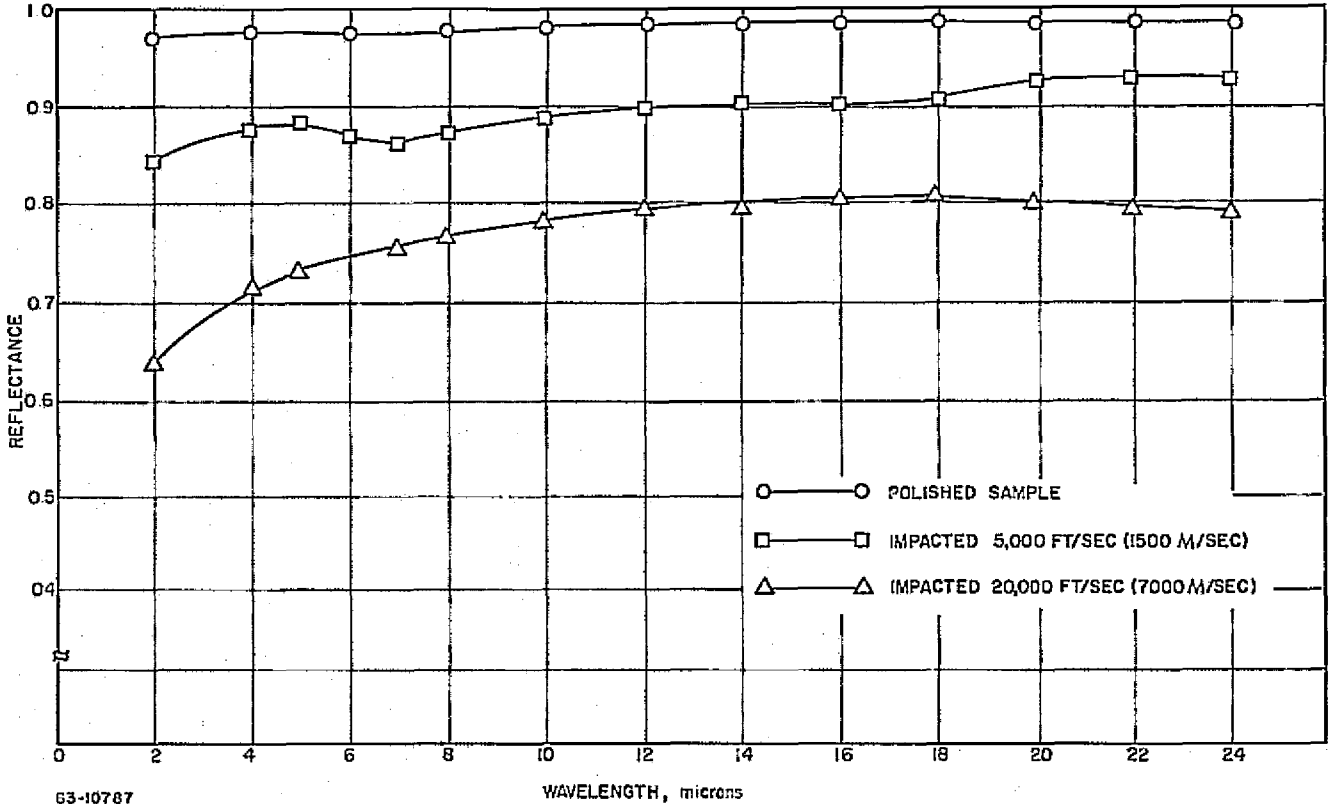

Figure 41 SPECTRAL REFLECTANCE OF SILVER

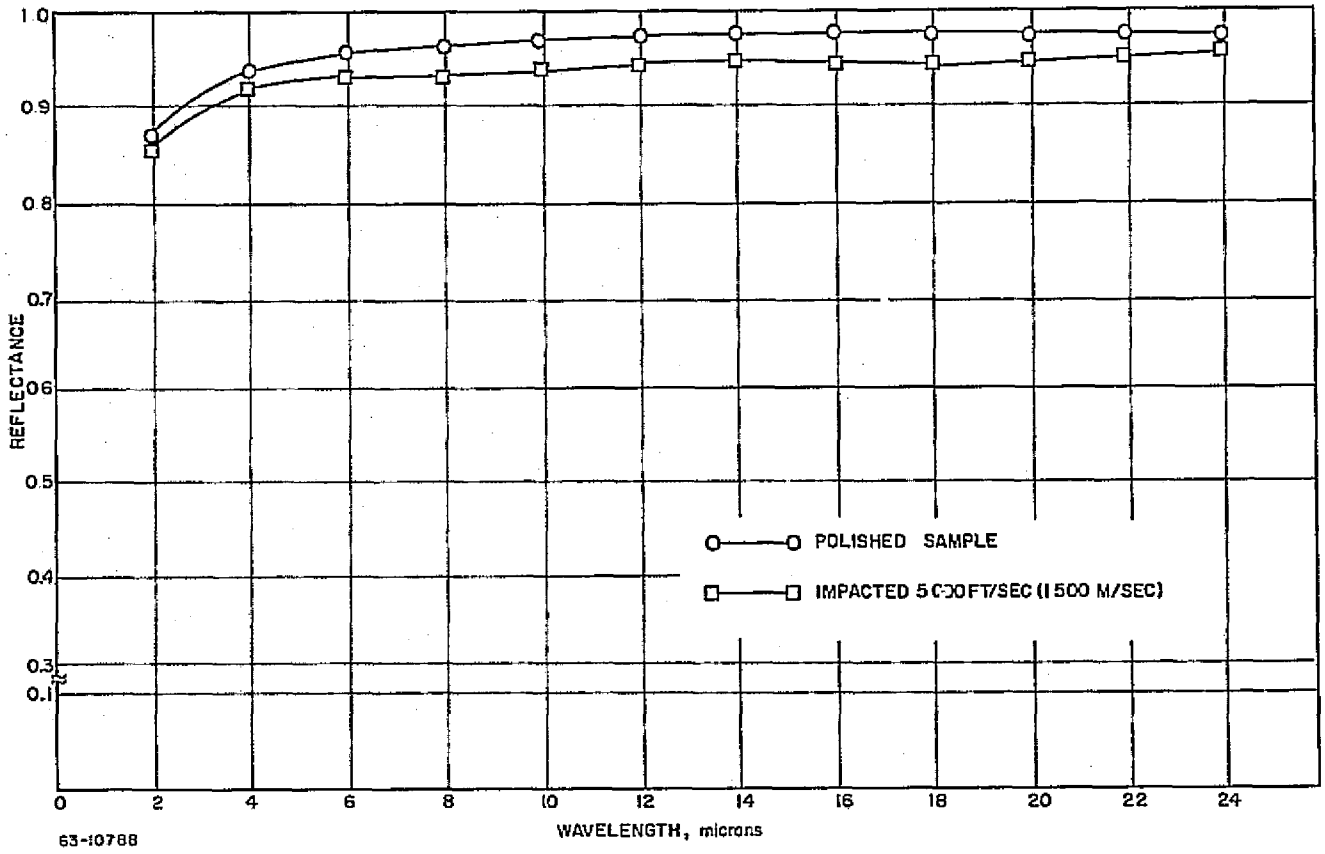

Figure 42 SPECTRAL REFLECTANCE OF TUNGSTEN

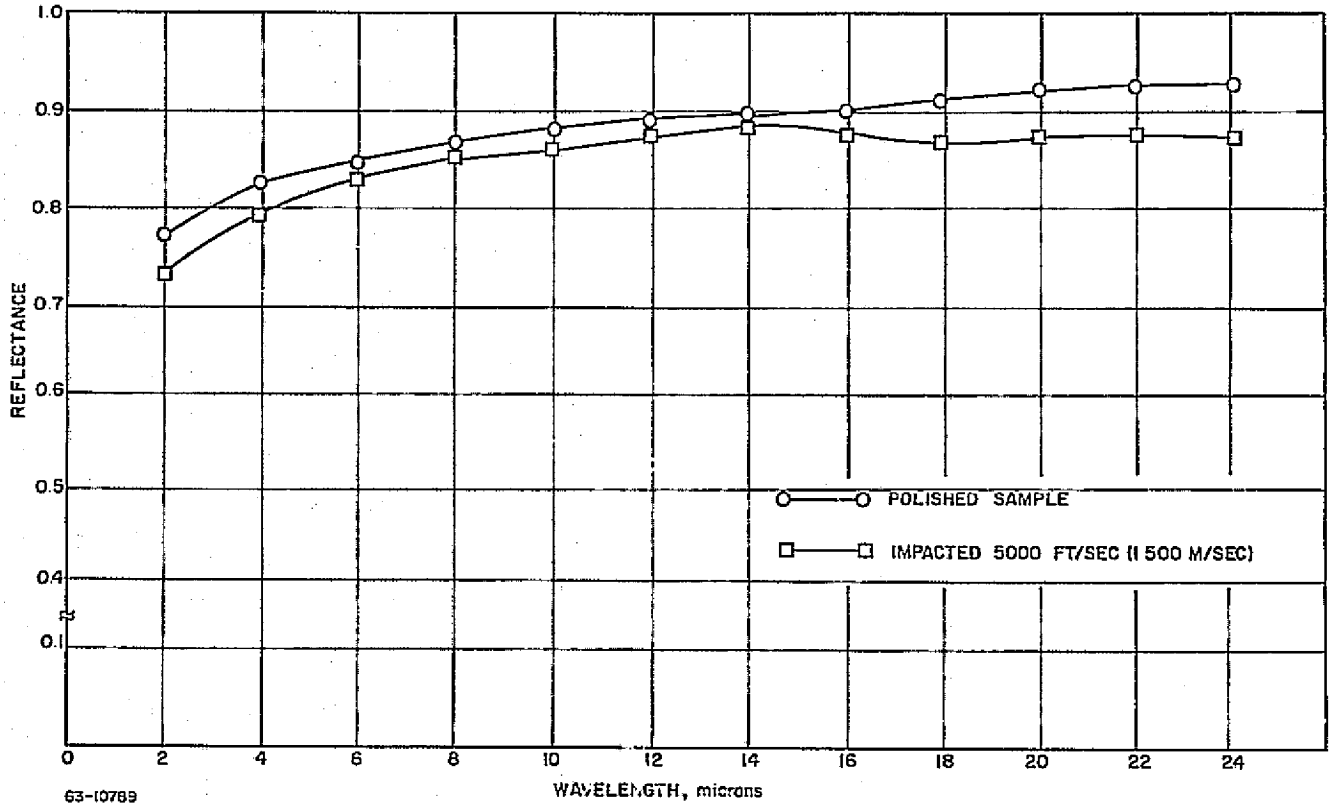

Figure 43 SPECTRAL REFLECTANCE OF STAINLESS STEEL, TYPE 316

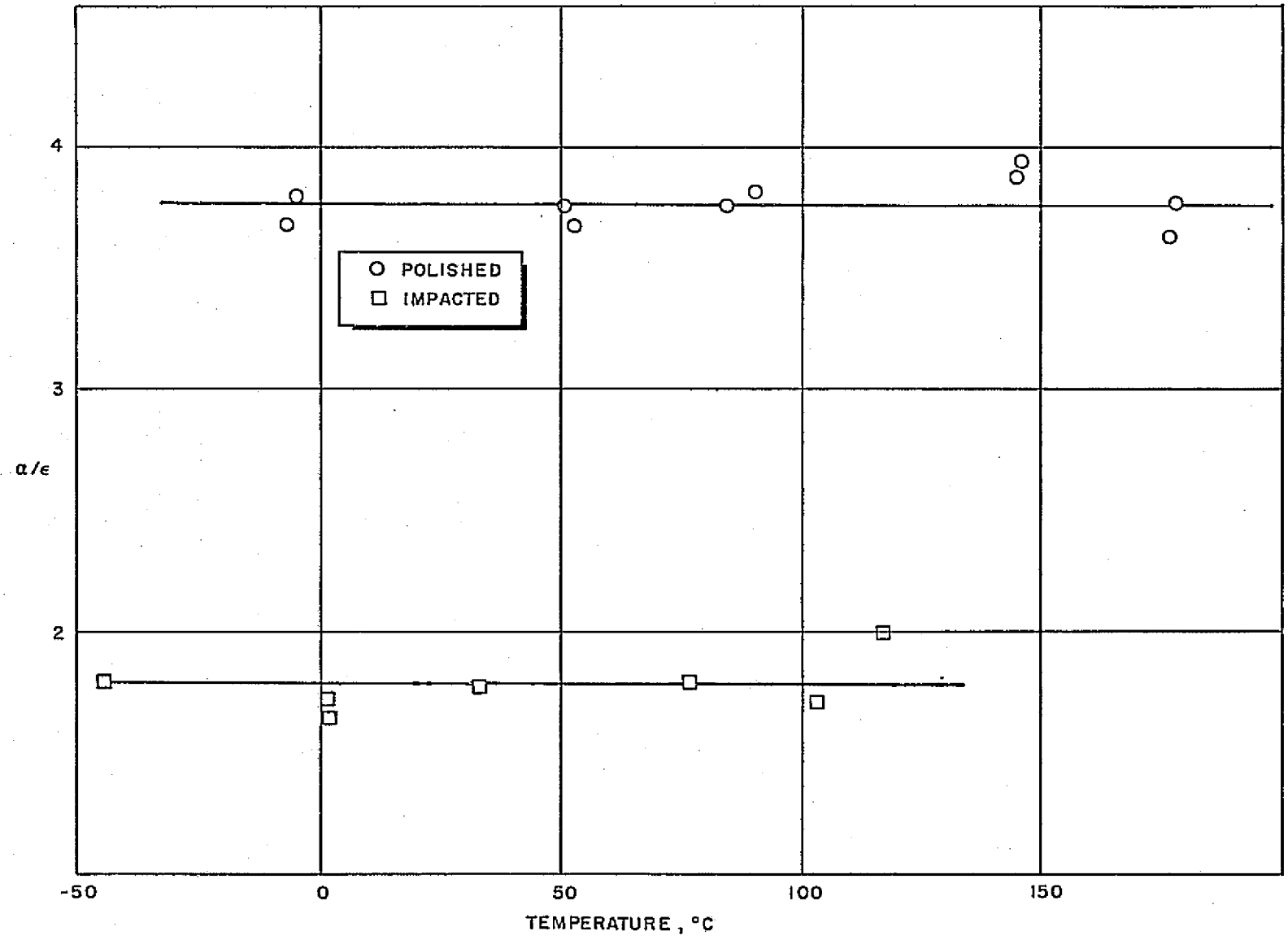

Figure 44 α/ϵ OF ALUMINUM
63-8010

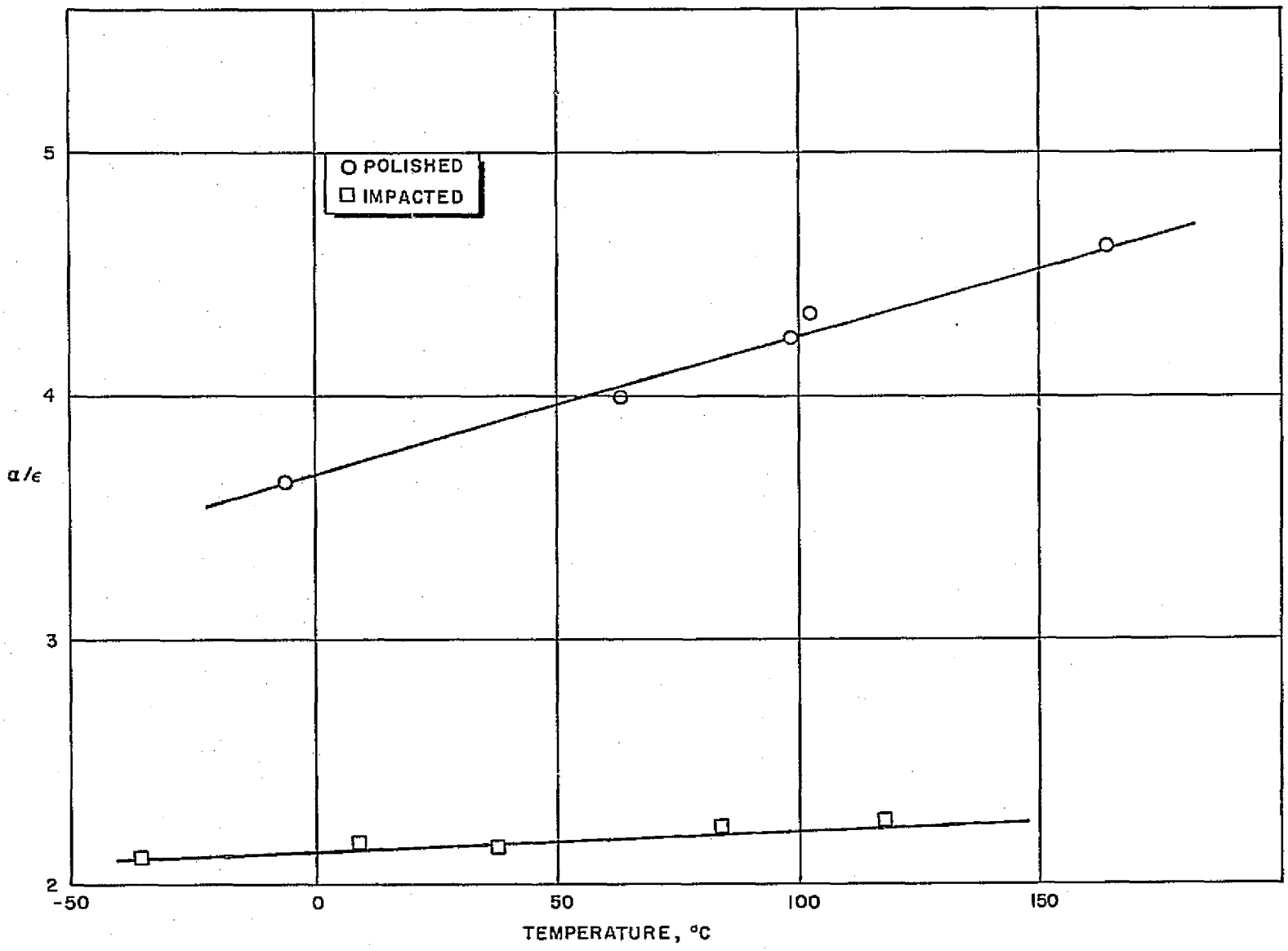

Figure 45 α/ε OF GOLD
63-8009

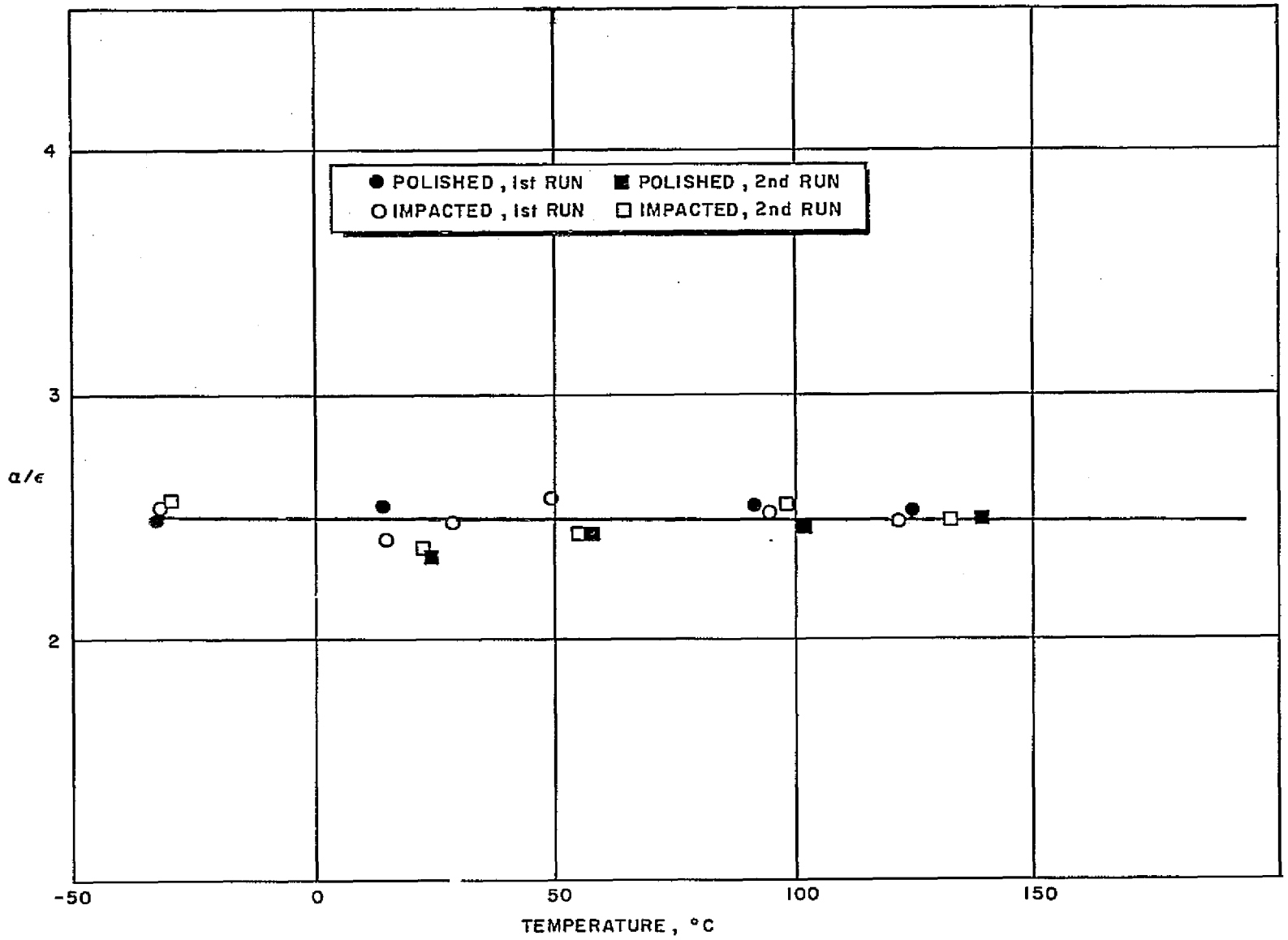

Figure 46 α/ε OF STAINLESS STEEL, TYPE 304
63-8007

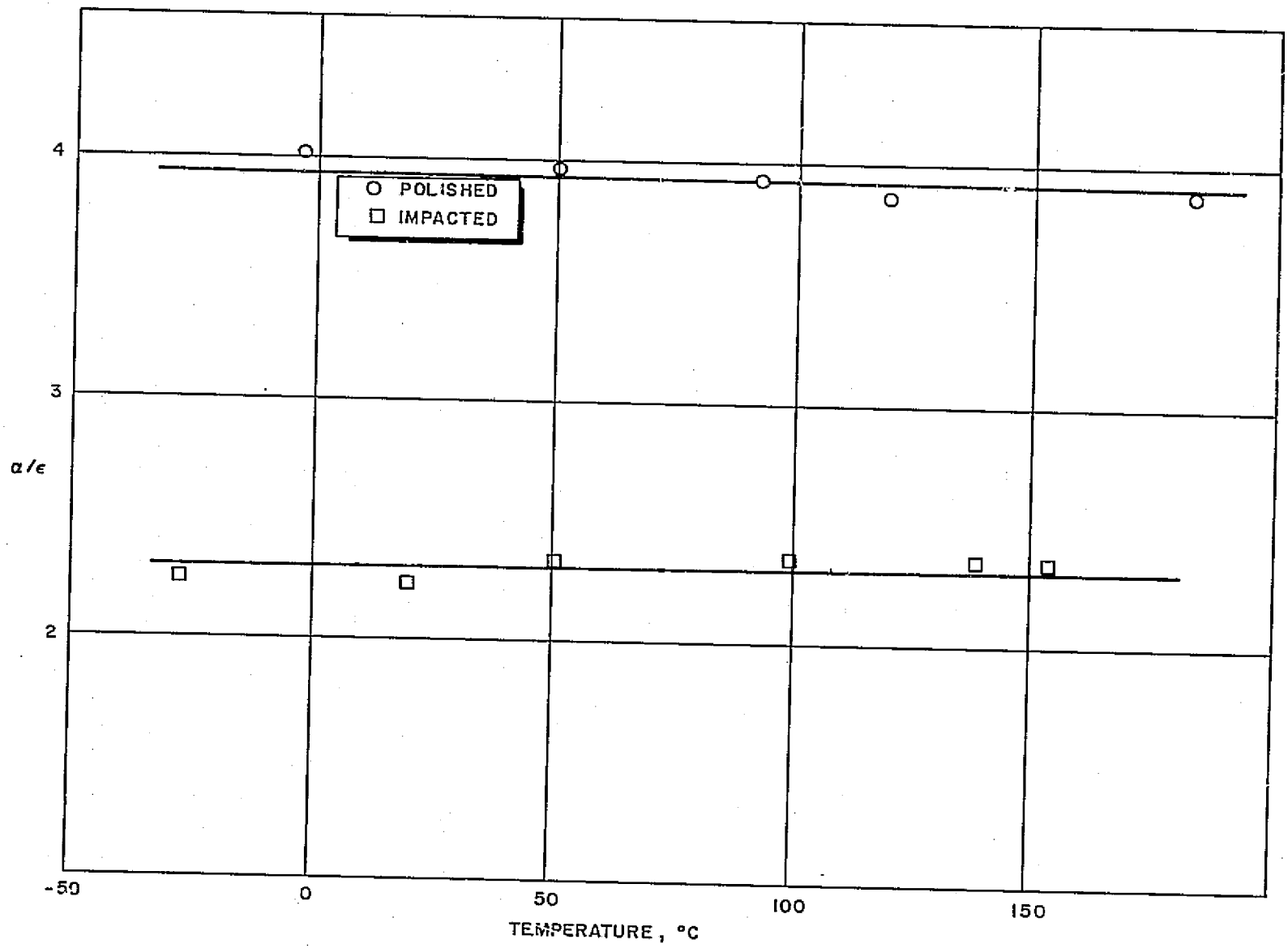

Figure 47 α/ε OF PLATINUM
63-8011

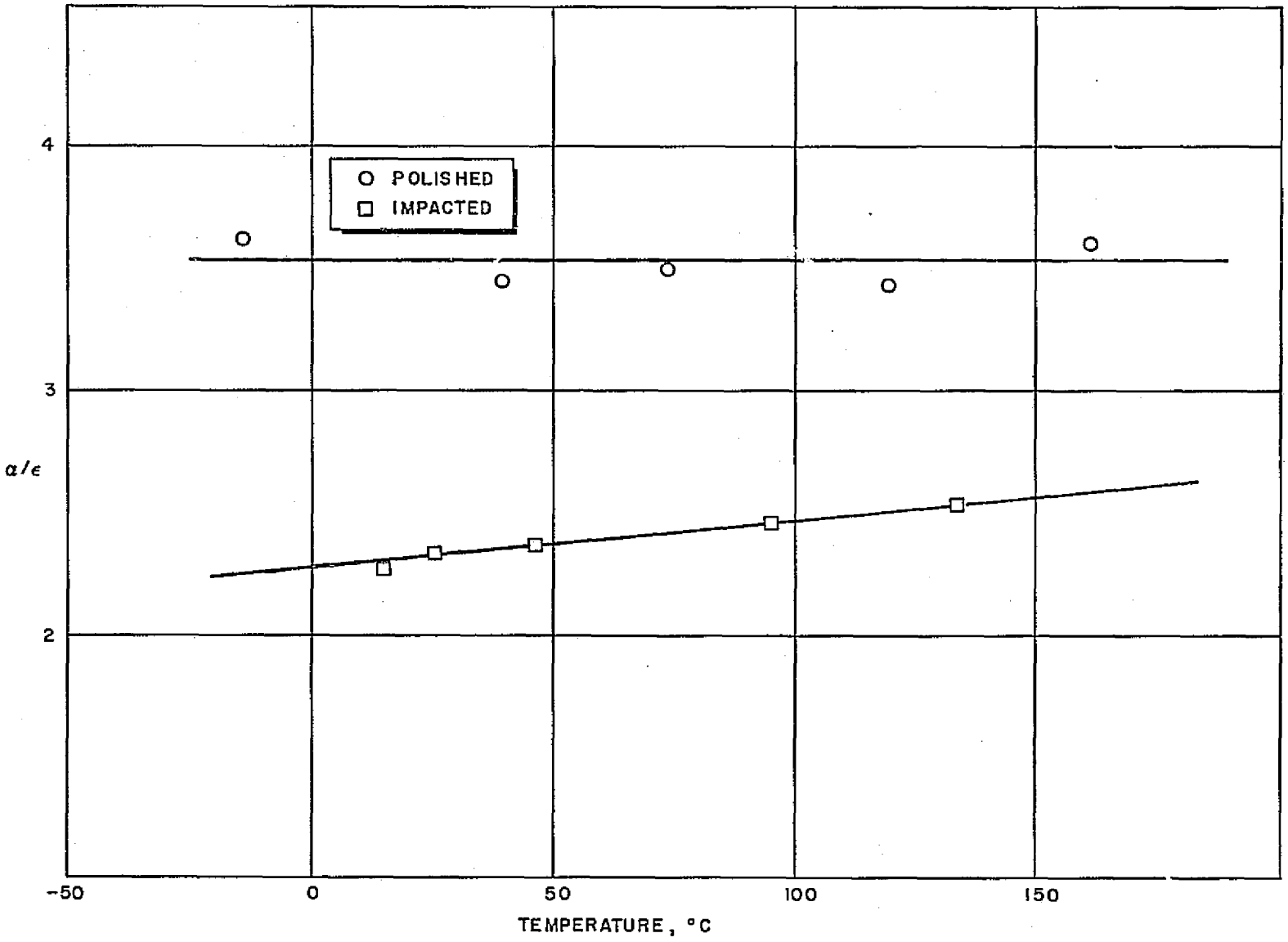

Figure 48 α/ϵ OF CHROMIUM-PLATED COPPER
63-8008

In observing changes in α/ϵ due to micrometeorite bombardment, the variation in the relation of two independent properties was measured. For analytical purposes, the direct measurement of each of the independent properties is more meaningful. For this reason, α and ϵ were determined independently by heating and cooling rate measurements as indicated in equations (8) and (9). The results of these rate measurements, giving α and ϵ of the specimens before and after impacting as well as their ratio, the change of each property, and their percentage change, are shown in table IV. The results show that, although the ratio of α to ϵ decreased in all cases, the individual values of both α and ϵ increased. The effective increase in both α and ϵ is most likely caused by the increase in surface area, a value which was not incorporated into the equations. Inclusion of the surface area increase in the calculations effectively normalizes the α and ϵ values and consequently would not indicate the change in the optical properties due to impacting.

Explanations, based on the increase in surface area or on Lambert's cosine law concerning the change in angular emittance with crater size and shape, can be advanced to account for the relatively large increases in ϵ as compared to the increases in α. Neither explanation, however, accounts for the apparent insensitivity of the α/ϵ of stainless steel.

In table V, the materials are arranged in order of decreasing percentage changes of α, ϵ, and surface area, average crater diameter, average crater depth, depth/diameter ratio and number of craters.

A direct correlation between these parameters cannot be established from the available data. Additional experiments involving controlled variations in the number, size, and depth of the craters are required to establish such a correlation.

TABLE IV

EFFECT OF MICROMETEORITE IMPACTS ON OPTICAL PROPERTIES

Material	α_o^*	α_i^*	$\Delta\alpha$	$\Delta\alpha/\alpha_o$ x 100 (percent)	ϵ_o^*	ϵ_i^*	$\Delta\epsilon$	$\Delta\epsilon/\epsilon_o$ x 100 (percent)	α_o/ϵ_o	α_i/ϵ_i	$\Delta\alpha/\epsilon$	$\Delta\alpha/\epsilon / \alpha_o/\epsilon_o$ x 100 (percent)
Aluminum	0.18	0.74	0.56	311	0.044	0.367	0.323	735	4.0	2.0	2.0	-50
Gold	0.27	0.63	0.36	133	0.047	0.250	0.203	440	6.0	2.5	3.5	-58
Platinum	0.24	0.68	0.44	183	0.059	0.336	0.277	470	4.0	2.0	2.0	-50
Chromium plated Copper	0.41	0.58	0.17	41	0.106	0.222	0.116	109	3.8	2.6	1.2	-32
Stainless Steel 304	0.23	0.42	0.19	83	0.084	0.167	0.083	98	2.8	2.5	0.3	-11

* α_o and ϵ_o refer to the measured α and ϵ values of the polished specimen and α_i and ϵ_i refer to the properties of the impacted specimens.

TABLE V

COMPARISON OF ORDERS OF OPTICAL AND SURFACE CHANGES

Order*	$\frac{\Delta a}{a_o}$	$\frac{\Delta \epsilon}{\epsilon_o}$	Number of Craters	Average Diameter	Average Depth	Depth Diameter	Area Damage
1	Al	Al	Al	Pt	Cr	Al	Pt
2	Pt	Pt	Au	Cr	Pt	Cr	Au
3	Au	Au	SS	SS	SS	SS	SS
4	SS*	Cr	Pt	Au	Al	Au	Al
5	Cr*	SS	Cr	Al	Au	Pt	Cr

*Order of 1 to 5 is order of decreasing magnitude

SS = stainless steel 304

Cr = chromium plated copper

III. CONCLUSIONS AND RECOMMENDATIONS

A. CONCLUSIONS

1. Bombardment by microprojectiles traveling at ~5,000 ft/sec (1500 m/sec) was observed to decrease the reflectance of various metals by 1 to 10 percent. Similar bombardment by microprojectiles traveling at ~20,000 ft/sec (7000 m/sec) caused decreases of 10 to 26 percent.

2. Bombardment by microprojectiles traveling at ~20,000 ft/sec (7000 m/sec) caused marked decreases in the solar absorption, thermal emittance ratio (α/ϵ) of four metals (Au, Pt, Al, Cr plated Cu) but did not affect the α/ϵ value of stainless steel 304.

3. Separate measurements of α and ϵ showed that in the cases where the α/ϵ value decreased, each of the two optical properties, α and ϵ, increased but that the increase in ϵ was greater. In the case of stainless steel 304, where the ratio remained constant, both α and ϵ were observed to increase at approximately the same rate.

B. RECOMMENDATIONS

It is recommended that these investigations be continued in the following direction.

1. It was found that for stainless steel 304, the α/ϵ value is the same for the highly polished metal and for the metal damaged by particle impact. The α/ϵ value for this metal was also found to be independent of the intensity of the radiation within the limits used in the measurements. This finding is very important in the selection of space vehicle skin material. With this material, the thermal energy through the vehicle wall and thus the thermal equilibrium within the vehicle would not be affected by the progressive change from a highly polished surface to a damaged surface. Before this information is applied, however, it must be substantiated by additional measurements.

Further, there is no reason to believe that this alloy is the only one exhibiting such behavior. Thus, it is recommended that the investigation be extended to other metals and alloys which, because of their other properties, can be considered for space vehicle skin material.

2. During the present work, only one impact density at each velocity has been applied to each investigated metal surface. At present, no definite knowledge is available on the micrometeorite density in space.

Should such information become available in the near future from actual measurements in space, the data obtained with the one impact density cannot be applied reliably to the actual values.

Thus, it is recommended that the measurement be performed at several impact density levels to develop a correlation between the change in α/ϵ and particle impact density.

3. The results so far obtained show that the reflectance, and consequently the emittance, of the investigated metals are greatly affected by an increase in the velocity of the impacting particles. The highest velocity used was 20, 000 ft/sec (7000 m/sec), a value considerably lower than the estimated velocity of micrometeorites in space. It appears to be important to continue these investigations by using particle velocities of 40, 000 to 50, 000 ft/sec (14, 000 to 17, 000 m/sec) to better simulate micrometeorite impacts. The resulting optical properties of the specimen will consequently be more representative of the optical properties of satellite skin materials exposed to micrometeorite impact in space.

Work at these high velocities may also reveal that the change in optical properties "diminishes" beyond a certain impact velocity. Therefore, it may not be necessary to further develop impacting techniques to attain the estimated velocity of micrometeorites in space.

4. Materials other than metals may also be considered as skin material. Several refractory compounds have better corrosion and erosion properties than metals. Further, there is a greater possibility to control the optical properties of such refractories. Work at RAD has shown that the emittance of some refractories is greatly increased by adding 1 percent of certain metal oxides. Such an addition should not adversely affect the refractory and mechanical properties of the system. Also, indications have been found that, for at least one pure refractory, the total normal emittance is independent of the surface finish.

Such refractories would very likely be applied as coatings on metal substrates. Thus, it is recommended to measure the α/ϵ value of such coatings in the freshly prepared and damaged condition.

5. Up until now, only a relatively minor effort has been made to correlate the observed changes in the optical properties with established radiation laws. To better understand these changes, attempts should be made to explain them on the basis of surface area changes and/or Lambert's cosine law, and to reconcile the changes with Hagen-Rubens radiation laws as well as with the Drude relationships.

IV. REFERENCES

1. Hass, G., I. F. Drummeter, and M. Schach, Temperature Stabilization of Highly Reflecting Spherical Satellites, J. Opt. Soc. Am. 49, 9 (September 1959) p. 918-924.

2. Jenness, J. R., The Effect of Surface Coatings on the Solar Radiation Equilibrium Skin Temperature of an Earth Satellite, Solar Energy, Vol 2 (October 1958), p. 17-20.

3. Acker, R. M., R. P. Lipkis, and J. E. Vehrencamp, Temperature Control System for the Atlas Able-4 Lunar Satellite, ASME Paper 60-Av-46 presented at the Aviation Conference of the ASME, Dallas (June 5 to 9, 1960).

4. Richmond, J. R., Coatings for Space Vehicles, First Symposium--Effects on Spacecraft Materials, (May 1959), edited by F. J. Clauss, Copyright 1960 by John Wiley and Sons, Inc.

5. Hopkins, A. K., The Meteoroid Hazard and Its Simulation, Symposium on the Effects of Space Environment on Materials, SAMPE, St. Louis (May 1962).

6. Birkebak, R., E. Sparrow, E. Eckert, and J. Ramsey, Effect of Surface Roughness on the Total Hemispherical and Specular Reflectance of Metallic Surfaces, ASME Paper 63-HT-6, Presented at Sixth National Heat Transfer Conference, Boston (August 1963).

7. Proceedings of Fourth Symposium on Hypervelocity Impacts, APGC-TR-60-39 (1), Air Proving Grounds, Center, ARDC, Elgin Air Force Base, Florida (April 1960).

8. Gier, J. T., R. V. Dunkle, and J. T. Bevans, J. Opt. Soc. Am., 44 (July 1954), p. 558-562.

9. Dunkle, R. V., F. Ehrenburg, and J. T. Gier, Spectral Characteristics of Fabrics from 1 to 23 Microns, Second National Heat Transfer Conference, ASME, AICHE (August 1959).

10. Gier, C. P., R. J. Jenkins, and W. J. Parker, Solar Absorptance and Total Hemispherical Emittance of Surfaces for Solar Energy Collection, ASD Technical Report 61-558 (February 1962).

11. Gaumer, R. E., Materials for Solar Energy Systems, Space Aeronautics 36 (October 1961) p. 60-65.

12. Gordon, G. D., Measurement of Ratio of Absorptivity of Sunlight to Thermal Emissivity, Rev. of Scientific Instruments 31 (11 November 1960), p. 1204-1208.

13. Butler, C. P. and E. C. Y. Inn, Surface Effects of Spacecraft Materials (May 1959), edited by F. J. Clauss, Copyright 1960 by John Wiley and Sons, Inc.

14. Gehring, J. W., An Analysis of Micro-Particle Cratering in a Variety of Target Materials, Proceeding of Third Symposium on Hypervelocity Impact Vol 1 (February 1959) p. 61-80.